

The opposition effect in the outer Solar System: a comparative study of the phase function morphology

Estelle Déau^{1, a}, Luke Dones^b, Sébastien Rodriguez^a,
Sébastien Charnoz^a and André Brahic^a

^a*CEA/IRFU/Service d'Astrophysique, AIM UMR 7158, 91191 Gif-sur-Yvette
FRANCE*

^b*Southwest Research Institute, 1050 Walnut Street, Suite 300 Boulder CO 80302,
USA*

Number of pages: 38

Number of tables: 5

Number of figures: 10

Running head: The opposition effect in the outer Solar System

¹ Corresponding author : Dr. Estelle DÉAU,

Address : CEA/IRFU/Service d'Astrophysique, Orme des Merisiers Btiment 709,
91191 Gif-sur-Yvette FRANCE,

e-mail estelle.deau@cea.fr, Phone +33(0)1 69 08 80 56, Fax +33(0)1 69 08 65 77

ABSTRACT

1

2 In this paper, we characterize the morphology of the disk-integrated phase
3 functions of satellites and rings around the giant planets of our Solar Sys-
4 tem. We find that the shape of the phase function is accurately represented
5 by a logarithmic model (Bobrov, 1970, in *Surfaces and Interiors of Planets*
6 *and Satellites*, Academic, edited by A. Dollfus). For practical purposes, we also
7 parametrize the phase curves by a linear-exponential model (Kaasalainen et al.,
8 2001, *Journal of Quantitative Spectroscopy and Radiative Transfer*, **70**, 529–
9 543) and a simple linear-by-parts model (Lumme and Irvine, 1976, *Astronom-*
10 *ical Journal*, **81**, 865–893), which provides three morphological parameters :
11 the amplitude A and the Half-Width at Half-Maximum (HWHM) of the oppo-
12 sition surge, and the slope S of the linear part of the phase function at larger
13 phase angles.

14 Our analysis demonstrates that all of these morphological parameters are cor-
15 related with the single scattering albedos of the surfaces.

16 By taking more accurately into consideration the finite angular size of the Sun,
17 we find that the Galilean, Saturnian, Uranian and Neptunian satellites have
18 similar HWHMs ($\lesssim 0.5^\circ$), whereas they have a wide range of amplitudes A .
19 The Moon has the largest HWHM ($\sim 2^\circ$). We interpret that as a consequence
20 of the “solar size bias”, via the finite size of the Sun which varies dramatically
21 from the Earth to Neptune. By applying a new method that attempts to mor-
22 phologically deconvolve the phase function to the solar angular size, we find
23 that icy and young surfaces, with active resurfacing, have the smallest values
24 of A and HWHM, whereas dark objects (and perhaps older surfaces) such as
25 the Moon, Nereid and Saturn’s C ring have the largest A and HWHM.

26 Comparison between multiple objects also shows that Solar System objects

27 belonging to the same planet host have comparable opposition surges. This
28 can be interpreted as a “planetary environmental effect” that acts to modify
29 locally the regolith and the surface properties of objects which are in the same
30 environment.

31 *keywords:* Planetary rings; Satellites of Jupiter, Saturn, Uranus, Neptune,
32 phase curves; opposition effect, coherent backscattering, shadowing, shadow-
33 hiding, angular size of the solar radius

34 1 Introduction

35 The opposition effect is a nonlinear increase of brightness when the phase an-
36 gle α (the angle between the source of light and the observer as seen from
37 the body) decreases to zero. This effect was seen for the first time in Saturn's
38 rings by Seeliger (1884) and Müller (1885). Now, this photometric effect has
39 been observed on many surfaces in the Solar System : first on satellites of
40 the giant planets, see (Helfenstein et al., 1997) for a review; second on aster-
41 oids, (Harris et al., 1989a,b; Belskaya and Shevchenko, 2000) and Kuiper Belt
42 Objects (Belskaya et al., 2008; Rozenbush et al., 2002); and finally on various
43 surfaces on Earth (Verbiscer and Veverka, 1990; Hapke et al., 1996) and for
44 minerals in the laboratory (Shkuratov et al., 1999; Kaasalainen, 2003). The
45 opposition effect on bodies in the Solar System has supplied interesting con-
46 straints about the regolith and state of the surfaces (Helfenstein et al., 1997;
47 Mishchenko et al., 2006). Indeed, the opposition effect is now thought to be
48 the combined effect of coherent backscatter (at very small phase angles), which
49 is a constructive interference between grains with sizes near the wavelength
50 of light, and shadow hiding (at larger phase angles), which involves shadows
51 cast by the particles themselves (Helfenstein et al., 1997).

52 By parametrizing the morphology of the phase functions for $\alpha \sim 0-20^\circ$, some
53 numerical models have derived physical properties of the medium in terms
54 of regoliths (Mishchenko and Dlugach, 1992a; Shkuratov et al., 1999) and the
55 state of the macroscopic surface (Hapke, 1986, 2002; Shkuratov et al., 1999).
56 However, such characterization of the phase function morphology is restricted
57 by the angular resolution and the phase angle range of the observed phase
58 function. Moreover, some effects (such as the finite size of the Sun and the

59 nature of the soil), which are not yet taken rigorously into account by the
60 most recent models, can play important roles in a comparative study.

61 For these reasons, it seemed important to test the behavior of the morphology
62 of the phase function before using any physical model.

63 The use of a simple morphological model is generally not adapted to derive
64 the physical properties of the medium. But for the data set presented here,
65 only the disk-integrated brightness I/F and the phase angle α are available,
66 the corresponding angles of incidence (i) and angles of emission (ϵ) are not
67 given for these observations, so we cannot use sophisticated for further inves-
68 tigation analytical models (Hapke, 1986, 2002; Shkuratov et al., 1999) which
69 need the brightness I/F and the three viewing geometry parameters α , μ and
70 μ_0 (μ and μ_0 are the cosines of ϵ and i , respectively).

71 However, the theories developed for the coherent-backscattering and the shadow-
72 hiding effects deduce their properties by parametrizing the opposition phase
73 curve (Mishchenko and Dlugach, 1992a,b; Mishchenko, 1992; Shkuratov et al.,
74 1999; Hapke, 1986, 2002). Thus it is possible to connect the morphological pa-
75 rameters A, HWHM and S with some physical characteristics of the medium
76 derived from these models.

77 The amplitude A of the opposition peak is generally known to express the
78 effects of the coherent-backscattering. According to Shkuratov et al. (1999);
79 Nelson et al. (2000), A is a function of grain size in such way that A decreases
80 with increasing grain size (we refer to grains as the smallest scale of the sur-
81 face compared to the wavelength and virtual entities implied in the coherent
82 backscatter effect, as microscopic roughness). This anti-correlation finds a nat-
83 ural explanation in the fact that for a macroscopic surface, large irregularities
84 with respect to the wavelength create less coherent effects than irregularities

85 with sizes comparable to the wavelength.
86 Mishchenko and Dlugach (1992b) and Mishchenko (1992) emphasize that A
87 is linked to the intensity of the background I_b (defined as a morphological pa-
88 rameter of the linear-exponential function of Kaasalainen et al., 2001), which
89 is a decreasing function of increasing absorption (Lumme et al., 1990); thus
90 A must increase with increasing absorption or decreasing albedo ϖ_0 , which
91 was confirmed by the laboratory measurements of Kaasalainen (2003). In-
92 deed, Kaasalainen (2003) remarked that the opposition surge increases and
93 sharpens when irregularities are small and that the opposition surge decreases
94 with increasing sample albedo.

95 The half width at half maximum HWHM, is also associated to the coherent-
96 backscatter effect. It has been related to the grain size, index of refraction, and
97 packing density of regolith, by previous numerical studies (Mishchenko, 1992;
98 Mishchenko and Dlugach, 1992a; Hapke, 2002). The variation of HWHM with
99 these three physical parameters is complex; see Fig. 9 of (Mishchenko, 1993):
100 HWHM reached its maximum for an effective grain size near $\lambda/2$ and increases
101 when the regolith grains' filling factor f increases. For high values of f , the
102 maximum of HWHM occurs for a larger grain size.

103 However, several studies Helfenstein et al. (1997); Nelson et al. (2000); Hapke
104 (2002) defined two HWHM parameters : for the Hapke (2002) model, the
105 coherent-backscatter HWHM (h_c), which is defined similarly to that in the
106 model of Mishchenko (1992), and the shadow hiding parameter h_s . Applying
107 this model to Saturn's rings, French et al. (2007) found that the coherent-
108 backscatter peak is about ten times narrower than the shadow-hiding peak,
109 but neither h_c nor h_s equals to the morphological width of the peak HWHM.
110 This reinforces the idea that a coupling of the two opposition effect mechanisms

111 at small phase angles could be responsible for the observed surge width.

112 Since the efficient regime of the shadow hiding is 10° – 40° (Buratti and Veverka,
113 1985; Helfenstein et al., 1997; Stankevich et al., 1999) and that of the co-
114 herent backscattering does not exceed several degrees (Helfenstein et al., 1997),
115 the slope of the linear part S can be regarded as the only parameter that mir-
116 rors the shadow hiding solely. This slope depends on the particle filling fac-
117 tor D , which relates to the porosity of the regolith of a satellite and the ratio
118 between the particle size and the physical thickness of the ring for a planetary
119 ring (Irvine, 1966; Stankevich et al., 1999; Kawata and Irvine, 1974). For a
120 satellite, by “particles” we mean the macroscopic scales of the surface, which
121 are implied in the shadow hiding effect.

122 In the shadowing model of Irvine (1966) and Kawata and Irvine (1974) (which
123 consists of the effects of shadows for a monolayer of particles), when the slope
124 is shallow, the variation of α does not change the visibility of shadows and the
125 particle filling factor must be high to make the proportion of shadows small
126 for any observation geometry. By contrast, when S is steep, the particle filling
127 factor is smaller and will contribute to a broad and large peak with a weak
128 amplitude which will be regarded as a slope.

129 In the shadow hiding model (i.e., multilayer shadowing), the larger the optical
130 depth and the volume density D , the steeper the phase function is at large
131 phase angles (10° – 40° , Stankevich et al., 1999). However, at larger phase an-
132 gles, the behavior of the absolute slope with albedo could change according
133 to a more efficient regime of the shadow hiding (50° – 90° , Stankevich 2008,
134 *private communication*).

135 For a compact medium such as a satellite’s surface, the slope at very large an-
136 gles ($\alpha > 90^\circ$) is a consequence of topographic roughness, the so-called rough-

137 ness parameter θ in the Hapke (1984, 1986) model. Then a steeper slope is
138 due to a surface tilt which varies from millimeter to centimeter scales (Hapke,
139 1984). However, the roughness can influence the phase curve at smaller phase
140 angles as underlined by Buratti and Veverka (1985), also according to the lab-
141 oratory measurements of Kaasalainen (2003), the slope of the phase function
142 ($\alpha < 40^\circ$) increases with increasing roughness. From the theoretical assertions
143 made above, the HWHM and the amplitude are governed by both coherent
144 backscatter and shadow hiding effects, whereas the slope of the linear part of
145 the phase curve is mirrors the unique expression of the shadow hiding effect.

146 The goal of this paper is to understand the role played by the two known op-
147 position effects (coherent backscatter and shadow hiding) on the morphology
148 of the surge for different surface materials, which have different values of grain
149 size, regolith grain filling factor, absorption factor (or inverse albedo), particle
150 filling factor and vertical extension, by making some comparisons with the
151 three morphological output parameters A , HWHM and S .

152 This paper describes the results of a full morphological parametrization and
153 comparison of phase functions of the main satellites and rings of the Solar
154 System in order to compare the influence of parameters not yet implemented
155 in actual models and simulations. Section 2 describes the data set that we
156 used here and the specific reduction we added to these previously published
157 data in order to compare them more easily. We also present the morphological
158 models that have supplied the parameters and discuss their link with physical
159 properties of the surfaces. In Section 3, we focus on the specific behaviors of
160 the morphological parameters, as a function of the single-scattering albedo,
161 the distance from the Sun and the distance from the center of the parent
162 planet. Section 4 is dedicated to a discussion in which we physically interpret

163 the general behaviors obtained with a deconvolution method. Conclusions and
164 future work that would be of interest are drawn in Sections 5.

165 **2 Data set description and reduction**

166 *2.1 The opposition effect around a selection of rings and satellites of the* 167 *giant planets*

168 We have applied a fitting procedure to a set of phase curves of satellites and
169 rings obtained by previous ground-based and *in situ* optical observations (see
170 Table 1 for references). The spectral resolution of the filters used for these
171 observations are not rigorously mentioned by their authors, and because we
172 mix for some objects phase curves of close wavelength, we give an approximate
173 value of the wavelength of observation (the uncertainty of the approximated
174 values is roughly 100 to 200 nanometers).

175 For a comprehensive study of the morphology of the opposition phase curves,
176 the solar phase curves of the Galilean satellites (Io, Europa, Ganymede and
177 Callisto) and the jovian main ring were chosen, as well as the phase curves of
178 the Saturnian rings (the classical A, B, and C rings and the tenuous E ring)
179 and some Saturnian satellites (Enceladus, Rhea, Iapetus and Phoebe); the
180 rings and satellites of Uranus [We refer to the seven innermost satellites of
181 Uranus – Bianca, Cressida, Desdemona, Juliet, Portia, Rosalind and Belinda
182 – as the Portia group, to follow the designation of Karkoschka (2001). The
183 phase function of the Portia group is then the averaged phase function for
184 these seven satellites.], including the Portia group and three other Uranian
185 satellites, Titania, Oberon and Miranda; and finally two Neptunian ring arcs

186 (Egalité and Fraternité) and two satellites of Neptune (Nereid and Triton).
187 For all the satellites of this study, the phase function is representative of the
188 leading side because they have, in general, better coverage at small phase
189 angles (except for Iapetus which have a trailing side brighter, we then use the
190 Iapetus' trailing side data). References for the phase curves that we use in this
191 study are given in table 1.

192 **Insert Table 1**

193 This study should give an extensive comparison between rings around the
194 giant planets (Jupiter, Saturn, Uranus and Neptune), as well as a comparison
195 between rings and satellites for each giant planet of our Solar System. For
196 practical purposes, the well-known phase curve of the Moon is added as a
197 reference.

198 *2.2 Data set reduction*

199 In order to properly compare the morphological parameters of the objects
200 whose phase curves are given as magnitudes, we have converted the magni-
201 tude M to the disk-integrated brightness I/F by using :

$$I/F = 10^{-0.4M} \quad (1)$$

202 (Domingue et al., 1995). This modification allows us to directly compare the
203 slope of the linear part of all the curves in the same unit.

205 The purpose of the present paper is to provide an accurate description of the
206 morphological behavior of the observed phase curves. This is the very first step
207 prior to any attempt to perform either analytical or numerical modeling. As
208 a consequence, special care has been given here to parametrizing the observa-
209 tions efficiently and conveniently. In addition, morphological parametrization
210 is necessary to efficiently compare numerous phase curves and derive statisti-
211 cal behavior, as will be done in Section 3.

212 Several morphological models have been used in the past to quantitatively
213 describe the shape of the phase functions : the logarithmic model of Bobrov
214 (1970), the linear-by-parts model of Lumme and Irvine (1976) and the linear-
215 exponential model of Kaasalainen et al. (2001). The specific properties of these
216 three models make them adapted for different and complementary purposes.
217 The logarithmic model is an appropriate and simple representation of the data,
218 the linear-by-parts model is convenient to describe the shape in an intuitive
219 way, and finally the linear-exponential model is commonly used for the phase
220 curves of Solar System bodies (see the comparative study of Kaasalainen et al.,
221 2001).

222 **Insert Fig. 1**

223 *2.3.1 The linear-by-parts model*

224 For an intuitive description of the main features of the phase curves, the linear-
225 by-parts model is the most convenient one. It is constituted of two linear
226 functions fitting both the surge at small phase angles ($\alpha < \alpha_1$) and the linear

227 regime at larger phase angles ($\alpha > \alpha_2$), where, generally, $\alpha_1 \neq \alpha_2$. Besides α_1
 228 and α_2 , this function depends on 4 parameters, A_0 , B_0 , A_1 , and B_1 , such that:

$$I/F(\alpha < \alpha_1) = -A_0 \cdot \alpha + B_0 \quad (2)$$

$$I/F(\alpha > \alpha_2) = -A_1 \cdot \alpha + B_1 \quad (3)$$

229 Lumme and Irvine (1976) and Esposito et al. (1979) use $\alpha_1=0.27^\circ$ and $\alpha_2=1.5^\circ$.
 230 By testing several values of α_1 , it appears that for our data set, values of
 231 $\alpha_1 = 0.5^\circ$ and $\alpha_2=2^\circ$ provide the best results, so these values are now adopted
 232 in the rest of the paper except for the Moon and tenuous rings for which we
 233 take $\alpha_1 = 1^\circ$.

234 In terms of the four parameters A_0 , B_0 , A_1 , and B_1 , the shape of the curve
 235 is characterized by introducing three morphological parameters : A, HWHM
 236 and S designating the amplitude of the surge, the half-width at half-maximum
 237 of the surge, and the absolute slope at “large” phase angles (i.e., a few degrees
 238 up to tens of degrees), respectively. The parameters are defined by :

$$A = \frac{B_0}{B_1} \quad \text{HWHM} = \frac{(B_0 - B_1)}{2(A_0 - A_1)} \quad \text{and} \quad S = A_1 \quad (4)$$

239 Even if all the part of the opposition curve cannot be fitted by two linear
 240 functions, this model offer a convenient description of the main trends of the
 241 phase curve.

242 2.3.2 *The linear-exponential model*

243 The linear-exponential model describes the shape of the phase function as a
 244 combination of an exponential peak and a linear part. Its main interest is that
 245 it has been used in previous work for the study of the backscattering part of the

246 phase curves of the Solar System’s icy satellites and rings (Kaasalainen et al.,
 247 2001; Poulet et al., 2002).

248 However, as noted by French et al. (2007), we find that this model does not
 249 fit the phase curves well: in particular A, HWHM and S are under- or over-
 250 estimated. In addition, the converging solutions found by a downhill simplex
 251 technique have large error bars, which means that a large set of solutions is
 252 possible and thus produce some difficulties for the comparison with the other
 253 objects.

254 For completeness, we give the four parameters of this model : the intensity
 255 of the peak I_p , the intensity of the background I_b , the slope of the linear
 256 part I_s and the angular width of the peak w such that the phase function is
 257 represented by :

$$I/F = I_b + I_s \cdot \alpha + I_p \cdot e^{-\frac{\alpha}{2w}} \quad (5)$$

258 As $\alpha \rightarrow 0$, $\exp(-\alpha/2w) \rightarrow 1 - \alpha/2w + \mathcal{O}(\alpha^2)$, so that the slope approaches
 259 $I_s + I_p/(2w)$. The degeneracy of these parameters may explain some of the
 260 difficulty in obtaining good fits described above. For consistency with previous
 261 work, we can express the amplitude and HWHM of the opposition surge in
 262 this model as:

$$A = \frac{I_p + I_b}{I_b} \quad \text{HWHM} = 2 \cdot \ln 2w \quad \text{and} \quad S = -I_s \quad (6)$$

263 We report in Table 2, the morphological parameters of the linear-by-parts
 264 model and that of the linear-exponential model.

265 **Insert Table 2**

266 *2.3.3 The logarithmic model*

267 As noted by Bobrov (1970), Lumme and Irvine (1976) and Esposito et al.
268 (1979), we remark that a logarithmic model describes the phase curves very
269 well. It depends on two parameters (a_0 and a_1). This model has the following
270 form :

$$I/F = a_0 + a_1 \cdot \ln(\alpha) \quad (7)$$

271 In general, this model is the best morphological fit to the data. However,
272 a_0 and a_1 are not easily expressed in terms of A, HWHM and S, since the
273 model's dependence on α is scale-free. Thus we report the values of these two
274 parameters in table 3 to allow an easier reproduction of the observational data.

275 *2.3.4 A method that takes into account the angular size of the Sun*

276 For all the phase curves presented here, a comparison of their surges could be
277 compromised because they have different values of their observed minimum
278 phase angle values. For example, data for the Galilean satellites never reach
279 0.1° , whereas data for Saturn's rings almost reach 0.01° .

280 Although the behavior within the angular radius of the Sun represents a small
281 part of the phase function, these smallest phase angles are crucial to constrain
282 the fit, especially for the linear-exponential model. Indeed, when $\alpha \rightarrow 0$, the
283 linear-exponential function tends toward $I_b + I_p/(2w)$; as a consequence, this
284 function flattens at very small phase angles.

285 However, in some cases this flattening does not correspond to the expected
286 flattening due to the angular size of the Sun because the linear-exponential

287 flattening fits itself arbitrarily with the phase angle coverage. The less points
288 there are at small phase angles, the sooner will occur the flattening of the
289 phase function.

290 Déau et al. (2008) showed for Saturn’s rings that the behavior of the surge was
291 accurately represented by a logarithmic model between 15° and 0.029° , where
292 0.029° corresponds to the angular size of the Sun at the time of the Cassini
293 observations. Below 0.029° , the resulting phase function flattens, whereas the
294 logarithmic function continues increasing. The use of this fact observed specif-
295 ically for Saturn’s rings and its generalization to the Solar System objects of
296 this study allows us to create extrapolated data points. Indeed, it is more con-
297 venient to use extrapolated data points than convolve the linear-exponential
298 function or the logarithmic function with the solar limb darkening. First be-
299 cause, for incomplete phase functions, the flattening of linear-exponential func-
300 tion is almost uncontrollable and second because for the logarithmic model,
301 even if a convolution is possible, linking the morphological parameters A ,
302 HWHM and S to the outputs a_0 and a_1 is not trivial.

303 The method to create extrapolated data points consists of first fitting the
304 logarithmic model to the data and then taking the value of the logarithmic
305 function at the phase angle which corresponds to the solar angular size (α_\odot ,
306 see Appendix). We then give to six points the same y -value : $I/F(\alpha = \alpha_\odot)$
307 and x -values ranging from 0.001° to α_\odot of phase angle. These extrapolated
308 data points are represented in Figure 2 (the full method is detailed in the Ap-
309 pendix). The extrapolated data and the original data are then fitted by the
310 linear-exponential model in the last step.

311 **Insert Fig. 2**

312 For the Moon, Ariel and Oberon, for which the phase curve has a few points

313 below the solar angular radius, we can see that the extrapolated points match
314 the observational points quite well. This proves that the solar angular size
315 effect is a flattening of the phase function below α_{\odot} . In the case of the HST
316 data for Saturn’s rings, for which we have also a few points below the solar
317 angular radius, the extrapolated points are a bit smaller than the observed
318 points. This is may be due to the fact that the data of French et al. (2007)
319 are already deconvolved by another method.

320 We also performed a convolution of the linear-exponential function to a limb
321 darkening function (see Appendix), but this refinement did not significantly
322 change the values of A, HWHM and S, because the linear-exponential model
323 already flattens as $\alpha \rightarrow 0$. Thus, by adding extrapolated data below α_{\odot} , we are
324 sure that the resulting fitting function will have a constant behavior below α_{\odot}
325 and that the resulting fitting function will take into account the angular size
326 of the Sun. However, we assume that all bodies have a logarithmic increase up
327 to the solar angular radius, which is only confirmed for Saturn’s rings. Output
328 parameters of our best fit for the “extrapolated linear-exponential” function
329 are given in table 3.

330 **Insert Table 3**

331 *2.3.5 A method of solar size deconvolution*

332 Although the behavior at phase angles smaller than the solar angular radius
333 represents a small part of the surge, a comparison of the surge of Solar Sys-
334 tem rings and satellites could be compromised because they have different
335 values for the mean solar angular radius ($\alpha_{\min}=0.051, 0.028, 0.014, 0.009^{\circ}$ re-
336 spectively for Jupiter, Saturn, Uranus and Neptune at their mean distances

337 from the Sun). Indeed, according to the results presented here, the amplitude
338 and HWHM seems linked to the finite angular size of the Sun. However, our
339 morphological study doesn't clearly show that the Sun's angular size effect is
340 preponderant for the amplitude A, because even considering more accurately
341 the "solar environmental effect," the surges of Neptune's satellites have smaller
342 amplitudes than those of Uranus (figure 8b). This contradicts the theoretical
343 assumption that the solar angular size would give the largest amplitude to the
344 most distant objects, for which the Sun has the smallest angular size. Because
345 we previously noted that the effect of the "solar environmental effect" was to
346 flatten the phase function when the phase angle is less than or equal to the
347 solar angular radius (Déau et al., 2008), a naive deconvolution method would
348 be to allow the phase curve to rise below α_{\odot} . This is also suggested by a pre-
349 vious deconvolution of HST data on Saturn's rings, for which the brightness
350 still increases below α_{\odot} (French et al., 2007). However, the linear-exponential
351 function is not appropriate for this purpose because it intrinsically flattens as
352 $\alpha \rightarrow 0$. Thus the only morphological function that allows an increase, even at
353 very small phase angles, is the logarithmic function. In particular, this function
354 allows the same increase of the brightness above and below the solar angular
355 radius (without break in the brightness), then using this function simulates a
356 point source of light. However, we assume that the smallest phase angles are
357 about $\alpha=0.001^{\circ}$, in this way, if a physical flattening should be performed by
358 the coherent backscattering or the shadow hiding effect, it will be possible at
359 these phase angles.

360 The logarithmic function fits the phase function quite well at small and large
361 phase angles (0.1-15°, Déau et al., 2008); however, none of the morphologi-
362 cal parameters A, HWHM and S are well-defined in this model. Because the
363 logarithmic model is a good representation of the data and perform a kind

364 of deconvolution at phase angles less than α_{\odot} , we fit this function by the
 365 linear-by-parts function. As shown in figure 3, the fitting results of this crude
 366 deconvolution method is reasonably acceptable when the phase function is
 367 plotted on a linear scale of phase angle.

368 **Insert Fig. 3**

369 However, on a logarithmic scale of α , the linear-by-parts fit is obviously not
 370 acceptable because intrinsically, a linear function cannot fit a logarithmic in-
 371 crease. As a consequence, we have slightly changed the linear-by-parts pa-
 372 rameters in order to take into account the inappropriate flattening of this
 373 function, compared to the logarithmic function. Because the y-intercept B_0 of
 374 the linear-by-parts model is less than the values of the logarithmic function
 375 when $\alpha < 0.01^\circ$, we replace B_0 by the value of the logarithmic function when
 376 $\alpha = 0.001^\circ$:

$$B'_0 = a_0 + a_1 \cdot \ln(10^{-3}), \quad (8)$$

377 where $a_1 \leq 0$, in such a way that the amplitude and the angular width are
 378 now given by :

$$A = \frac{B'_0}{B_1} \quad \text{and} \quad \text{HWHM} = \frac{(B'_0 - B_1)}{2(|a_1| - A_1)} \quad (9)$$

379 where $|a_1|$ is the absolute slope of the logarithmic function (see section 2.3.3).
 380 Replacing $|a_1|$ by A_0 in the formula for HWHM was motivated by the fact that
 381 the original values of the linear-by-parts parameters were systematically the
 382 same (HWHM $\sim 0.22^\circ$ for $\alpha_1 = 0.3^\circ$). This is due to the fact that the logarithmic

383 function is a fractal function, so it is not possible to obtain a Half-Width at
384 Half Maximum. Values of the linear-by-parts parameters A, HWHM and S
385 are given in Table 5. Our best result is probably that for the B ring, for which
386 we previously found different values of A from the Franklin and Cook (1965)
387 data and the French et al. (2007) data (A=1.30 and A=1.38 respectively, see
388 table 2 with the convolved models). The discrepancy was still present with the
389 extrapolated linear-exponential model (A=1.35 for Franklin and Cook (1965)
390 and A=1.32 for French et al. (2007)), due to the fact that the solar angular
391 size was different at the two observation times (see table Appendix 6). Now,
392 with the unconvolved model, the discrepancy of the two values is somewhat
393 reduced compared to values from the fit to the original data : A=1.82 for
394 Franklin and Cook (1965) and A=1.77 for French et al. (2007), table 5, which
395 implies that the angular size effect is now absent.

396 **Insert Table 5**

397 **3 Results**

398 Our procedure is to interpret more carefully the morphological results of a
399 large dataset. We start first by studying the behaviors of the morphological
400 parameters with the single scattering albedo with the raw data (Section 3.1
401 and 3.2) and the improved data that take into account of the solar size of the
402 Sun (Section 3.3). In a last step, we freed from the solar size bias by trying to
403 look the opposition effect in the outer Solar System with the same solar size,
404 assumed to be a point (Section 3.4).

405 *3.1 Behaviors of the morphological parameters*

406 In this section we compare the morphological parameters as a function of the
407 single scattering albedo ϖ_0 .

408 Since the single scattering albedo ϖ_0 represents the ratio of scattering effi-
409 ciency to total light extinction over the phase angle range (Chandrasekhar,
410 1960), its value must be computed with the largest coverage of phase angle as
411 possible (0 to 180 degrees). This is why we did not compute the single scatter-
412 ing albedo with the phase curves presented in this paper but we use previously
413 published values of single scattering albedo computed from phase curves with
414 a larger phase angle coverage than ours and a wavelength close to ours. Thus,
415 references for phase curves (table 1) and references for ϖ_0 (table 4) are not
416 always the same.

417 **Insert Table 4**

418 We did not found single scattering albedo values for the jovian main ring and
419 the Saturn's E ring, so these two objects will be excluded of the study of the
420 morphological parameters with the single scattering albedo.

421 *3.1.1 Variation of the angular width of the surge with albedo*

422 First, we discuss the variation of $\text{HWHM}=f(\varpi_0)$ derived from the linear-by-
423 parts model (Figure 4a) and $\text{HWHM}=f(\varpi_0)$ derived from the extrapolated
424 linear-exponential model (Figure 4b). Interestingly, the variation differs ac-
425 cording to the morphological model : the first case leads to a decrease of
426 HWHM when ϖ_0 increases, while the latter case leads to an increase of HWHM
427 when ϖ_0 increases.

428 **Insert Fig. 4**

429 The different results for $\text{HWHM}=f(\varpi_0)$ between the linear-by-parts results
430 (well fitted by $\text{HWHM}\sim 0.9 \times 0.3^{\varpi_0}$, Figure 4a) and the extrapolated linear-
431 exponential results (represented by $\text{HWHM}\sim 0.15 + 0.19\varpi_0$, Figure 4b) is
432 mainly due to the points which correspond to the Moon, Callisto and Nereid.
433 Indeed, in general, values from the extrapolated linear-exponential model sig-
434 nificantly decrease for the outer Solar System objects, whereas the value for
435 the Moon increases by almost 1° . This is due to the fact that when we take
436 into account the Sun's angular size, this effect lower the values of HWHM for
437 the incomplete phase functions.

438 However, Figure 4 shows a large dispersion of HWHM with albedo.

439 *3.1.2 Variation of the amplitude of the surge with albedo*

440 Figure 5 shows a weak dependence of the amplitude of the surge on the albedo
441 for the satellites, already noted by Helfenstein et al. (1997); Rozenbush et al.
442 (2002).

443 **Insert Fig. 5**

444 In both cases (linear-by-parts model, Figure 5a and extrapolated linear-exponential
445 model, Figure 5b) we note a dependence of A with ϖ_0 , which follow a function
446 leading to a decrease of A when ϖ_0 increases ($A\sim 1.65 \times 0.72^{\varpi_0}$ in Figure 5a
447 and $A\sim 1.75 \times 0.72^{\varpi_0}$ in Figure 5b). The consistent trends in both cases im-
448 ply that the finite size of the Sun was correctly derived by the linear-by-parts
449 model.

450 The decrease of A with increasing ϖ_0 could be understood by a relation be-

451 tween the amplitude and the single scattering albedo via the intensity of the
452 background phase function I_b (with the linear-exponential model), which is in-
453 versely proportional to the albedo. Thus, the predicted trend of Lumme et al.
454 (1990) is confirmed by our present results.

455 In addition, Figure 5b labels satellites by color to indicate their parent planet.
456 This figure indicates that distant objects (such as the Uranian satellites) have
457 a significantly larger amplitude than less distant objects (such as the Galilean
458 or Saturnian satellites) while the Neptunian satellites have values in the av-
459 erage. Then it must be considered that the finite size of the Sun has a role in
460 the amplitude's value (Shkuratov, 1991). As a consequence, even if the trend
461 of $A=f(\varpi_0)$ is well explained by theoretical considerations, one can remark
462 that the large dispersion in this correlation could be due to other effects (such
463 as the finite size of the Sun) that weakens the albedo dependence of A. Thus,
464 as for HWHM, we cannot physically interpret the variation of HWHM and A
465 as long as they are convolved with the effect of the solar angular size.

466 *3.1.3 Variation of the slope of the linear part with albedo*

467 The last morphological parameter is the slope S, which we represent as a func-
468 tion of the single scattering albedo ϖ_0 for the rings (Figure 6a) and satellites
469 (Figure 6b) of the Solar System.

470 **Insert Fig. 6**

471 In this figure, rings and satellites have different values of slope as function
472 of their albedo, and a slight increase for S with increasing ϖ_0 is noticed. For
473 the rings (Figure 6a), it seems that a good correlation appears between S and
474 the albedo, which may be roughly fitted by a function like $S \sim 0.001 + 0.02 \cdot \varpi_0^2$.

475 A similar fit works well for the satellites (the Moon, Saturnian and Uranian
476 satellites are not far from the dashed line in figure 6b). This fit to the points
477 could be $S \sim 0.001 + 0.01 \cdot \varpi_0^2$ (Figure 6b). However, three objects fall far from
478 this curve : Europa, Ganymede and Io. This correlation suggests that multiple
479 scattering may be a strong element at play in the regime of self-shadowing
480 (beyond $\sim 1^\circ$ of phase angle), in qualitative agreement with Kawata and Irvine
481 (1974).

482 *3.2 Cross comparisons between the morphological parameters of the surge*

483 We see in Figure 4 that the angular width of the surge can change significantly
484 by taking into account the solar angular radius. However, it is not the case for
485 the amplitude of the surge (Figure 5). Figure 7 shows the behavior of a cross
486 comparison between the morphological parameters A and HWHM obtained
487 with the linear-exponential model convolved (Figure 7b) or not (Figure 7a)
488 with the limb darkening function.

489 **Insert Fig. 7**

490 In the first graph (Figure 7a), it first seems that two different groups may be
491 qualitatively distinguished.

492 On the one hand, there is a group of objects with similar values of the HWHM,
493 in the range 0.1° to 0.4° , but with significantly different values of the ampli-
494 tude, from 1.4 to 1.8. It is interesting to note that these bodies, which include
495 the Saturnian rings and Uranian satellites, are not bodies in the outermost
496 part of the Solar System (such as the Neptunian satellites). Within this group,
497 we also note that similar objects are gathered in the (A,HWHM) space: the

498 Uranian satellites have, on average, the largest values of the amplitude, ~ 1.7 .
499 Saturn's rings have an amplitude between 1.3 and 1.6, closer to the Uranian
500 satellites. We also note that whereas all satellites have quite a constant HWHM
501 (between 0.2° and 0.4°), Saturn's rings have systematically lower values, be-
502 tween 0.08° and 0.09° , which may be suggestive of a different state of their
503 surface.

504 The second group includes Saturn's satellites, along with Io, Europa and Tri-
505 ton, which have the lowest values of amplitude. A very striking feature is the
506 peculiar behavior of bodies such as Callisto and the Moon : they have similar
507 amplitudes (about 1.5) and also similar HWHMs (about 2°). In the second
508 graph (Figure 7b), it first seems that the bodies belonging to the same pri-
509 mary planet have similar values of A and HWHM. For the Galilean satellites,
510 we found the largest HWHM for the outer Solar System satellites (between
511 0.2° and 0.5°) and amplitude between 1.1 and 1.5. The Uranian satellites still
512 have the largest amplitudes (A ranges between 1.6 and 1.9), but the values
513 of HWHM are similar to that of those of Saturn's rings and satellites. The
514 Neptunian satellites have the sharpest opposition peaks ($\text{HWHM} \lesssim 0.1^\circ$) but
515 moderate amplitudes (between 1.2 and 1.4), similar to the range of the Sat-
516 urnian satellites.

517 Does this imply some deep structural difference of the surface regolith of bod-
518 ies, or is it due to the Sun's angular size effect? For the moment we note that
519 the opposition effect is poorly understood, especially at phase angles smaller
520 than 1° in the coherent backscattering regime.

521 Whereas physical implications are still hard to draw from these graphs, it is
522 interesting to note that the solar angular size refinement that we use naturally
523 clusters different kind of surfaces in different locations of the (A, HWHM)
524 space, and that "endogenically linked objects" are quite well gathered in small

525 portions of this space. This could suggest that common environmental pro-
526 cesses (meteoroid bombardment, surface collisions, space weathering, etc.) may
527 homogenize different surface states by processing mechanisms that may deter-
528 mine the microstructure of the surface, and then, in turn, the behavior of
529 the opposition surge at very low phase angles, as it may be linked with the
530 spatial organization of micrometer-scale surface regolith (Mishchenko, 1992;
531 Mishchenko and Dlugach, 1992a; Shkuratov et al., 1999).

532 *3.3 Additionnal effect*

533 With the cross comparison of the morphological parameters of the surge, the
534 angular size of the Sun and the fact that objects seem “endogenically linked”,
535 two supplementary effects (observationnal and physical) can significantly mod-
536 ify the values of A and HWHM : the “solar size bias” and the “planetary
537 environmental effect”.

538 *3.3.1 The “solar size bias”*

539 We tested the influence of the solar angular size by representing in Figure 8
540 the morphological parameters of the surge A and HWHM as a function of the
541 distance from the Sun d (in Astronomical Units).

542 **Insert Fig. 8**

543 We represent HWHM (Figure 8a) and A (Figure 8b) from the linear-by-parts
544 model with filled symbols and that of the extrapolated linear-exponential
545 model with empty symbols.

546 We remark that the linear-by-parts angular width follows the power-law func-

547 tion $\text{HWHM} \sim 0.33 + 1.1d^{-1.5}$ (the solid line in Figure 8a). The fit is quite good
548 from the Moon to Uranus, but is far from the values of Neptune's satellites
549 (especially that of Nereid). It is easier to see with this representation that
550 the HWHM of Nereid is larger than that expected by the power-law function.
551 The extrapolated linear-exponential HWHM corrects this because the Nep-
552 tunian satellites now have smaller values of HWHM that are better fitted by
553 the power-law function. Indeed, the extrapolated linear-exponential HWHM
554 follows a similar function ($\text{HWHM} \sim 0.12 + 2.3d^{-1.4}$), but values at the extreme
555 parts of the Solar System (innermost with the Earth's satellite and outermost
556 with Neptune's satellites) are significantly different : for the Moon, the extrap-
557 olated linear-exponential HWHM is larger than its linear-by-parts counterpart
558 and for the Nereid, the extrapolated linear-exponential HWHM is smaller than
559 the linear-by-parts HWHM.

560 However, such a strong trend is not observed in the case of the amplitude
561 of the surge. As shown in Figure 8b, a fit to the linear-by-parts amplitudes
562 is good for the Galilean, Saturnian and Uranian satellites (which we fit by a
563 linear function $A \sim 1.1 + 0.08d$) but not at all for the Moon and the Neptunian
564 satellites. The predicted behavior (dashed line in Figure 8b) shows that the
565 value for the Moon is overestimated and that the values of the Neptunian
566 satellites are strongly underestimated. The use of values of the extrapolated
567 linear-exponential A did not improve the fit. Indeed, the extrapolated linear-
568 exponential amplitude is larger than the linear-by-parts amplitude for the
569 Moon, whereas the extrapolated linear-exponential values of the Neptunian
570 satellites are smaller than their linear-by-parts counterparts. The exact op-
571 position trends were expected to obtain a good linear fit from the Moon to
572 Neptune. Perhaps the solar size effect is not important at Neptune's distance
573 and the values of A and HWHM are physical, in the sense that they depend

574 only on the opposition effect mechanisms (coherent backscattering and shadow
575 hiding).

576 These results seems to suggest that A is less affected by the “solar size bias”
577 than HWHM, which is entirely controlled by this effect (which seems trivial
578 because this bias is an angular effect). It is possible that the values of A result
579 from a coupling of the physical opposition effects (coherent backscatter and
580 shadow hiding) with the environmental opposition effects (solar and plane-
581 tary). As a consequence, the deconvolution of the phase function (at least for
582 the “solar size bias”) should allow the physical opposition effects to express
583 fully themselves in the values of A and HWHM.

584 3.3.2 *The “planetary environmental effect”*

585 Previous studies by Bauer et al. (2006) and Verbiscer et al. (2007) have con-
586 firmed, at the scale of the Saturnian system, a kind of “endogenic” or “ecosys-
587 temic” classification of the opposition surge. Indeed, these works demonstrated
588 that the opposition surge paramaters of the outermost and innermost Satur-
589 nian satellites, respectively, can be a function of the distance from Saturn.

590 For the planetary environments of Jupiter, Uranus and Neptune, there is no
591 significant variations with distance from the parent planet. The first reason is
592 maybe statistical because there are not enough data to make (for these sys-
593 tems, we have less than four objects). The second is that the dust environment
594 can be influenced by other effects (the magnetospheric activity, the satellite’s
595 activity, the proximity to the Kuiper Belt and transneptunian objects), in such
596 way that the distance from the planet host could be irrelevant for some of the
597 planetary environments.

598 For the Saturnian system, for which local interactions between satellites and

599 rings exists, we observe similar trends with our results than the trends of
600 Bauer et al. (2006) and Verbiscer et al. (2007) (see Figure 9).

601 **Insert Fig. 9**

602 Variations of the morphological parameters on large scales of distance (for the
603 Saturn system) show trends that suggest a common ground for environmental
604 processes. These processes may imply different surfaces, but will be handled
605 by the opposition effect in the same way by the mechanisms that determine
606 the microstructure of the surface. According to theoretical models of coherent
607 backscattering, the amplitude is related to the grain size and HWHM depends
608 on the composition, distribution of grain size and the regolith filling factor.
609 Thus the behavior of the opposition surge is connected to the spatial organiza-
610 tion of the regolith (Mishchenko and Dlugach, 1992a; Shkuratov et al., 1999).
611 Therefore, the study of the morphology of the opposition peak can highlight
612 dynamical interactions between the rings, satellites and the surrounding en-
613 vironment through the photometry. These ring/satellite interactions noticed
614 here go beyond the general dynamical interactions between rings and satel-
615 lites (such as resonances, for example). Here these interactions involve common
616 erosion histories on the surfaces of the rings and satellites. Similar values of
617 HWHM according to the theory of Mishchenko and Dlugach (1992a) can be
618 explained by similar values of refractive index (with various values of grain
619 size and filling factor), or by different values of refractive indices, but similar
620 values of grain sizes and filling factor of the regolith.

621 There are two known mechanisms that can act together in order to explain the
622 similarities in the values of HWHM for objects that are *endogenically linked*.

623 ① The impacts of debris in planetary environments can change the chem-
624 ical composition of the rings and satellites : new elements can be directly

625 added to the system ; the more volatile elements can be preferentially re-
626 moved and the more fragile compounds can be preferentially processed. The
627 work of Cuzzi and Estrada (1998), in particular, details changes in the chem-
628 ical composition of Saturn’s rings by meteoroid bombardment and ballistic
629 transport.

630 ② The second mechanism that is likely to act concerns every kind of colli-
631 sional mechanism capable of modifying, at microscopic scales, the surface of
632 the satellite’s regolith (meteoroid bombardment, external collisions, disinte-
633 gration in space, etc.); see (Lissauer et al., 1988; Colwell and Esposito, 1992,
634 1993). In the case of ring particles, models of erosion by ballistic transport
635 have been developed and predict the destruction of micrometer-sized grains in
636 dense rings ($\tau > 1$), see (Ip, 1983).

637 *3.4 Study of the unconvolved opposition parameters*

638 With the unconvolved morphological parameters obtained with the method
639 in Section 2.3.5, we are now sure that the morphological surge parameters are
640 independent of the distance from the Sun, and thus independent of the “solar
641 size bias”. Indeed, in Figure 10, we represent A and HWHM derived from the
642 linear-by-parts model which fits the logarithmic model as a function of the
643 distance from the Sun and there is no relation with the distance, unlike in
644 Figure 8.

645 **Insert Fig. 10**

646 Moreover, we can see that three groups can be distinguished :

647 (1) A group with the Moon, Callisto, the C ring, Phoebe, the classical Uranian

648 satellites (Ariel, Titania and Oberon) and Nereid. They have large angular
649 widths and amplitudes ($\text{HWHM} \gtrsim 0.5^\circ$, Figure 10a and $A \gtrsim 2.0$, figure 10b).
650 We can see that these objects are dark, with low and moderate albedos (ta-
651 ble 4). These objects are also known to be heavily cratered (Neukum et al.,
652 2001; Zahnle et al., 2003); thus, they don't have intrinsic resurfacing mech-
653 anisms. For the specific case of the resurfacing of the Saturn's C ring, it
654 is known that the collisional activity of a ring is controlled by the opti-
655 cal depth τ (Cuzzi and Estrada, 1998). The number of collisions per orbit
656 per particle is proportional to τ (in the regime of low optical depth, see
657 Wisdom and Tremaine, 1988), and the random velocity in a ring of thick-
658 ness H is about $H \times \Omega$ (with Ω standing for the local orbital frequency).
659 Since H is a decreasing function of τ , impact velocities are high in regions
660 of low optical depth. As a result, particles in low optical depth regions (such
661 as the C ring) may suffer of resurfacing characterized by rare, but somewhat
662 higher-speed, collisions.

663 (2) A group with Io, Iapetus, Rhea and the bright Saturnian rings character-
664 ized by smaller amplitude and angular width : $A \lesssim 1.7$ and $\text{HWHM} \sim 0.4^\circ$
665 (figures 10a,b).

666 (3) A group with Ganymede, Europa, Enceladus and Triton with the smallest
667 amplitude and angular width ($1.3 < A < 1.6$, Figure 10a and $0.1 < \text{HWHM} < 0.3^\circ$,
668 Figure 10b). Interestingly for the amplitude, we can see that this group con-
669 tains only the brightest surfaces of the Solar System, with a single scattering
670 albedo close to $\varpi_0 \sim 0.9$ (however, Bond albedo of Ganymede is quite lower,
671 see Squyres and Veverka, 1981). These objects are also known to have active
672 resurfacing. Indeed, this was confirmed for Europa, which has a very young
673 surface and perhaps recent geyser-like or volcanic activity (Sullivan et al.,
674 1998; Pappalardo et al., 1998b), and Ganymede, on which the grooved ter-

675 rains could have formed through tectonism, probably combined with icy vol-
676 canism (Pappalardo et al., 1998a; McCord et al., 2001). Present-day resur-
677 facing is also taking place on Enceladus, whose geysers produce the E ring
678 (Porco et al., 2006), and for Triton, which also has geysers (Croft et al.,
679 1995).

680 This classification seems to suggest that the darkest and oldest surfaces have
681 the largest amplitudes for the surge and that the brightest and youngest sur-
682 faces have the smallest amplitudes. However, one might be surprised that the
683 third group does not include Io, which has an intense resurfacing via tidally
684 induced volcanism. Also, the Portia group does not belong to only one group
685 in figure 10 : it belongs to the group 3 for HWHM and to the group 2 for
686 the amplitude A. For these two isolated cases, it is possible that the average
687 of photometric phase curves from different satellites is responsible of the fact
688 that Io and the Portia group are difficult to classify.

689 4 Discussion

690 4.1 Implications of the surge parameters of the unconvolved data

691 By removing the “solar size bias”, we can try to physically interpret the am-
692 plitude variations with the single scattering albedo with the mechanisms pro-
693 posed to explain the opposition effect. Our study shows a link between the
694 single scattering albedo and the unconvolved morphological parameters. A
695 linear fit to the unconvolved amplitude is $A=2.2 - 0.5\varpi_0$ (with a correlation
696 coefficient of -61%) and the linear fit to the unconvolved angular width is
697 $HWHM=0.52 - 0.19\varpi_0$ (with a correlation coefficient of -38%). By excluding

698 the Portia group, we find a better correlation coefficient for HWHM : -66%.
699 These correlations are stronger than that previously found with the convolved
700 data. This shows that the “solar size bias” acts to scatter the morphologi-
701 cal parameters. As a consequence, the fact that old and dark surfaces with a
702 low resurfacing activity have high unconvolved amplitude whereas the bright
703 and young surfaces with an intense resurfacing activity have low unconvolved
704 amplitude is linked to the single scattering albedo variations of A. Indeed
705 the single scattering albedo is a measure of the brightness of a surface. But
706 not only: according to Shkuratov et al. (1999), the amplitude of the coherent
707 backscattering opposition surge is a decreasing function of increasing regolith
708 grain size. If the morphological amplitude is due to the coherent backscattering
709 effect (Mishchenko and Dlugach, 1992b; Mishchenko et al., 2006), the depen-
710 dence of $A = f(\varpi_0)$ could be understood as a positive correlation between
711 the grain size and the single scattering albedo. However, it is possible that the
712 morphological amplitude is not only that of the coherent backscattering effect
713 but is dominated by both effects : coherent backscatter and shadow hiding, as
714 underlined by Hapke (2002). However, here it is not possible to separate the
715 two effects and say which effect is dominant because to separate the coher-
716 ent backscatter and shadow hiding mechanisms, the polarization is required
717 (Muinonen et al., 2007).

718 *4.2 Implications of the slope of linear part*

719 The strong correlation of the slope S (in I/F.deg⁻¹ units) with single scat-
720 tering albedo (Figure 6) implies that shadow hiding is more efficient in high
721 albedo surfaces. This trend was previously remarked in the opposition slope

722 of asteroids by (Belskaya and Shevchenko, 2000). It was first interpreted by
723 these authors as a decrease of the absolute slope with albedo, consistent with
724 the analytical model of Helfenstein et al. (1997) which predicted that the am-
725 plitude of the shadow hiding must decrease with albedo. However, because the
726 slope unit in (Belskaya and Shevchenko, 2000) is magnitude (remark that the
727 scale of the magnitude is not reversed for their graph, figure 4, as for the the
728 other graphes that show the phase curves, figures 1 and 2), a decreasing slope
729 in mag.deg^{-1} corresponds to an increasing slope in $I/F.\text{deg}^{-1}$ units. As a con-
730 sequence, the behavior of the slope as a function of the albedo for the rings,
731 satellites and asteroids of the Solar System is consistent and all lead to the
732 same idea that shadow hiding is reinforced at high albedo. The correlation be-
733 tween slope and albedo seems to be the strongest trend of the opposition effect
734 in satellites and rings of the Solar System and the use of more sophisticated
735 models is needed to understand them.

736 The results from Figure 6 are in agreement with the simulations of ray-tracing,
737 (Stankevich et al., 1999), which models shadow hiding in a layer of particles.
738 These simulations show that shadow hiding creates a linear part in the phase
739 function from 10 to 40 degrees and that the absolute slope of the linear part
740 becomes steeper when optical depth increases and the filling factor of the layer
741 of particles increases.

742 How does albedo relate to the optical depth and the filling factor? Previous
743 studies have shown that the albedo and optical depth are highly positively
744 correlated for the rings, (see Doyle et al., 1989; Cooke, 1991; Dones et al.,
745 1993). For satellites, optical depth is effectively infinite; since this removes one
746 variable, relating the slope parameter to the nature of the surface is easier for
747 satellites than for rings. Thus we must consider two kinds of objects:

- 748 • For rings, where the optical depth is finite, variation of the slope S will be
749 a subtle effect involving both optical depth and filling factor ;
- 750 • For satellites, which have “solid” surfaces, variations in slope are linked to the
751 filling factor of each surface. If the optical depth is invariant for satellites,
752 according to the model of Stankevich et al. (1999), only variations of the
753 filling factor can explain differences in the slope S . However, the notion of
754 filling factor is not well suited for satellites; indeed, a description involving
755 a topographical roughness is more appropriate.

756 We noticed that when the optical depth is finite, as for the rings, the ef-
757 fects of slope are stronger with a high albedo than for high albedo satellites.
758 Consequently the shadow hiding effect for the ring is more efficient than for
759 satellites and reflects a difference between the three-dimensional aspect of a
760 layer of particles in the rings and a planetary regolith.

761 **5 Conclusion**

762 The goal of this paper was to understand the role of the viewing conditions
763 on the morphological parameters of the opposition surge and the role played
764 by the single scattering albedo on the morphological parameters. We have use
765 three methods to fit the data: the first one with a simple morphological model,
766 secondly by taking more accurately into account the role of the size of the Sun
767 in the morphological model and thirdly eliminating the role of the size of the
768 S_{in} in the morphological model.

769 The results of this study allow us to highlight several facts related to the
770 observation and the mechanisms of the opposition effect in the Solar System.

771 (1) The slope of the linear part is an increasing function of albedo. Our results
772 are consistent with those of Belskaya and Shevchenko (2000), for which the
773 slope of the phase function of asteroids increases when albedo increases.
774 These results confirm the predictions from simulations of shadow hiding for
775 the first time.

776 (2) We note that the morphological parameters of the surge (A and HWHM)
777 are sensitive to the phase angle coverage, specifically to the smallest phase
778 angles. We have extrapolated observational data points in order to correct
779 the lack of data near the solar angular radius. However, this method needs
780 to be improved, for example by taking directly into account of the solar
781 angular radius in the linear-exponential function. We hope that future data
782 at the smallest phase angles, will confirm the extrapolated data that we use
783 to perform the “extrapolated linear-exponential” model.

784 (3) The amplitude and the angular width of the opposition surge are linked
785 to the single scattering albedo of the surfaces, as already noted in labo-
786 ratory measurements (Kaasalainen, 2003). Like Belskaya and Shevchenko
787 (2000), we believe that the single scattering albedo is one of the key el-
788 ements constraining morphological parameters. However before physically
789 interpreting these results, A and HWHM need to be deconvolved to the “so-
790 lar size bias” since we have a large dispersion in the relations of $A = f(\varpi_0)$
791 and $\text{HWHM} = f(\varpi_0)$.

792 (4) By deconvolving the phase functions to the Sun’s angular size effect, we
793 showed that A and HWHM are still correlated with the albedo (with better
794 correlation coefficients). The dependence of A and HWHM are now inde-
795 pendent of the distance from the Sun, unlike their convolved counterparts.
796 Indeed, values of A and HWHM from deconvolved phase functions can be
797 classified into three groups that include a mix of bodies from the inner and

798 the outer Solar System. This shows that icy and young surfaces (such as
799 Europa, Io, Enceladus and Triton) have the smallest amplitudes, whereas
800 dark and older surfaces (such as the Moon, Phoebe and the C ring) have
801 the largest amplitudes.

802 (5) It seems that two effects (the “solar size bias” and the “planetary environ-
803 mental effect”), act together to disperse data taken from different places in
804 the Solar System. Moreover, with our technique of deconvolution of phase
805 curves, we see that the “solar size bias” can be removed from A and HWHM,
806 because unconvolved data have A and HWHM that don’t show any trend
807 with distance from the Sun. These arguments strengthen the conclusions
808 that the notion of “ecosystem” for a planetary environment can be the key
809 element determining the opposition effect surge morphology.

810 Our method cannot directly derive the physical properties obtained from the
811 models. Firstly, because there is a large set of models and it seemed more
812 convenient to separate the morphological models from the more physical and
813 sophisticated ones. Secondly, because the various spectral resolution of our
814 data set is not appropriate for a majority of physical models which need a fine
815 spectral resolution (for example, in the coherent backscatter theory, HWHM
816 is linked to the ratio of the wavelength over the free mean path of photons). In
817 addition, the coherent backscatter can significantly polarized the brightness
818 of a surface (??), so the polarized phase curves can bring crucial and comple-
819 mentary informations to that of the unpolarized phase curves. Consequently,
820 more investigations need to be provided for this purpose by using color and
821 polarized phase curves.

822 For a future work, which will critically depend on the quality of the observa-
823 tions, first it would be interesting to study the phase functions of the lead-

824 ing and trailing faces of synchronously rotating satellite in order to test the
825 role of the environmental effect more precisely. Indeed, satellites are sub-
826 ject to energy fluxes from electrons, photons and magnetospheric plasma,
827 and ion bombardment, which are not the same on the leading and trailing
828 sides (Buratti et al., 1988). Consequently, morphological parameters might
829 vary significantly from the leading side to the trailing side for the same satel-
830 lites. However, the important dispersion in trailing side data (see for example
831 Kaasalainen et al., 2001) did not allow us to pursue this comparison. We then
832 hope to have in the future that more accurate data of all satellites of the satel-
833 lites of the Solar System.

834 Secondly, to better understand the role of the “planetary environmental effect,”
835 a more relevant study would be the comparison of rings with “ringmoons” or
836 small satellites which are in the vicinity of the rings. Several examples of such
837 a ring/ringmoon system are present in the environment of each giant planet :

- 838 • for Jupiter : Metis and Adrastea with the main ring (Showalter et al., 1987);
839 Amalthea and Thebe with the Gossamer ring (Burns et al., 1999) ;
- 840 • for Saturn : Pan, Daphnis and Atlas with the outer A ring (Smith et al.,
841 1981; Spitale et al., 2006), Prometheus and Pandora with the F ring (Smith et al.,
842 1981), and Enceladus with the E ring (although Enceladus is the primary
843 source of the E ring, it is usually not called a “ringmoon” (Verbiscer et al.,
844 2007) ;
- 845 • for Uranus : Cordelia and Ophelia with the ϵ ring (French and Nicholson,
846 1995) ;
- 847 • for Neptune : Galatea with the Adams ring (Porco, 1991).

848 Unfortunately, opposition phase curves of the small satellites are not actually
849 available because they require a fine spatial resolution.

Acknowledgements

The authors would like to thank S. Kaasalainen and D. French for kindly providing us with some of the solar phase curves used here, as well as J. Burns, K. Muinonen and D. Stankevich for useful comments that improved the quality of the paper. This work was supported by the French Centre National de la Recherche Scientifique and the Cassini project.

References

- Bauer, J. M., Grav, T., Buratti, B. J., Hicks, M. D., Sep. 2006. The phase curve survey of the irregular saturnian satellites: A possible method of physical classification. *Icarus* 184, 181–197.
- Belskaya, I. N., Levasseur-Regourd, A.-C., Shkuratov, Y. G., Muinonen, K., 2008. Surface Properties of Kuiper Belt Objects and Centaurs from Photometry and Polarimetry. *The Solar System Beyond Neptune*, pp. 115–127.
- Belskaya, I. N., Shevchenko, V. G., Sep. 2000. Opposition Effect of Asteroids. *Icarus* 147, 94–105.
- Blanco, C., Catalano, S., Jun. 1974. On the photometric variations of the Saturn and Jupiter satellites. *Astronomy & Astrophysics* 33, 105–111.
- Bobrov, M. S., 1970. Physical properties of Saturn’s rings. In: *Surfaces and interiors of planets and satellites*, edited by A. Dollfus (Academic, New York). pp. 376–461.
- Buratti, B. J., Sep. 1984. Voyager disk resolved photometry of the Saturnian satellites. *Icarus* 59, 392–405.
- Buratti, B. J., 1985. Photometry of rough planetary surfaces : The role of multiple scattering. *Icarus* 64, 320–328.
- Buratti, B. J., Gibson, J., Mosher, J. A., Oct. 1992. CCD photometry of the Uranian satellites. *Astronomical Journal* 104, 1618–1622.
- Buratti, B. J., Lane, A. L., Gibson, J., Burrows, H., Nelson, R. M., Bliss, D., Smythe, W., Garkanian, V., Wallis, B., Oct. 1991. Triton’s surface properties - A preliminary analysis from ground-based, Voyager photopolarimeter subsystem, and laboratory measurements. *Journal of Geophysical Research Supplement* 96, 19197–+.
- Buratti, B. J., Nelson, R. M., Lane, A. L., May 1988. Surficial textures of the

- Galilean satellites. *Nature* 333, 148–151.
- Burns, J. A., Showalter, M. R., Hamilton, D. P., Nicholson, P. D., de Pater, I., Ockert-Bell, M. E., Thomas, P. C., May 1999. The Formation of Jupiter’s Faint Rings. *Science* 284, 1146–+.
- Chandrasekhar, S. 1960. Radiative transfer. New York (Dover).
- Colwell, J. E., Esposito, L. W., Jun. 1992. Origins of the rings of Uranus and Neptune. I - Statistics of satellite disruptions. *Journal of Geophysical Research* 97, 10227–+.
- Colwell, J. E., Esposito, L. W., Apr. 1993. Origins of the rings of Uranus and Neptune. II - Initial conditions and ring moon populations. *Journal of Geophysical Research* 98, 7387–7401.
- Cooke, M. L., 1991. Saturn’s rings: Photometric studies of the C Ring and radial variation in the Keeler Gap. Ph.D. thesis, AA(Cornell Univ., Ithaca, NY.).
- Croft, S. K., Kargel, J. S., Kirk, R. L., Moore, J. M., Schenk, P. M., Strom, R. G., 1995. The geology of Triton. In: Neptune and Triton. pp. 879–947.
- Cuzzi, J. N., Estrada, P. R., Mar. 1998. Compositional Evolution of Saturn’s Rings Due to Meteoroid Bombardment. *Icarus* 132, 1–35.
- Déau, E., Charnoz, S., Dones, L., Brahic, A., Porco, C. C., 2008. ISS/Cassini observes the opposition effect in Saturn’s rings: I. Morphology of optical phase curves. *Icarus* *submitted* in April 2007 and corrected in May 2008.
- de Pater, I., Gibbard, S. G., Chiang, E., Hammel, H. B., Macintosh, B., Marchis, F., Martin, S. C., Roe, H. G., Showalter, M., Mar. 2005. The dynamic neptunian ring arcs: evidence for a gradual disappearance of Liberté and resonant jump of courage. *Icarus* 174, 263–272.
- Domingue, D., Verbiscer, A., Jul. 1997. Re-Analysis of the Solar Phase Curves of the Icy Galilean Satellites. *Icarus* 128, 49–74.

- Domingue, D. L., Lockwood, G. W., Thompson, D. T., Jun. 1995. Surface textural properties of icy satellites: A comparison between Europa and Rhea. *Icarus* 115, 228–249.
- Dones, L., Cuzzi, J. N., Showalter, M. R., Sep. 1993. Voyager Photometry of Saturn's A Ring. *Icarus* 105, 184–215.
- Doyle, L. R., Dones, L., Cuzzi, J. N., Jul. 1989. Radiative transfer modeling of Saturn's outer B ring. *Icarus* 80, 104–135.
- Esposito, L. W., Lumme, K., Benton, W. D., Martin, L. J., Ferguson, H. M., Thompson, D. T., Jones, S. E., Sep. 1979. International planetary patrol observations of Saturn's rings. II - Four color phase curves and their analysis. *Astronomical Journal* 84, 1408–1415.
- Ferrari, C., Brahic, A., Sep. 1994. Azimuthal brightness asymmetries in planetary rings. 1: Neptune's arcs and narrow rings. *Icarus* 111, 193–210.
- Franklin, F. A., Cook, A. F., Nov. 1974. Photometry of Saturn's satellites - The opposition effect of Iapetus at maximum light and the variability of Titan. *Icarus* 23, 355–362.
- Franklin, F. A., Cook, F. A., Nov. 1965. Optical properties of Saturn's rings. II. Two-color phase curves of the 2 bright rings. *Astronomical Journal* 70, 704–+.
- French, R. G., Nicholson, P. D., May 1995. Edge waves and librations in the Uranus epsilon ring. In: *Bulletin of the American Astronomical Society*. Vol. 27 of *Bulletin of the American Astronomical Society*. pp. 857–+.
- French, R. G., Verbiscer, A., Salo, H., McGhee, C., Dones, L., Jun. 2007. Saturn's Rings at True Opposition. *The Publications of the Astronomical Society of the Pacific* 119, 623–642.
- Hapke, B., Jul. 1984. Bidirectional reflectance spectroscopy. III - Correction for macroscopic roughness. *Icarus* 59, 41–59.

- Hapke, B., Aug. 1986. Bidirectional reflectance spectroscopy. IV - The extinction coefficient and the opposition effect. *Icarus* 67, 264–280.
- Hapke, B., Jun. 2002. Bidirectional Reflectance Spectroscopy⁵. The Coherent Backscatter Opposition Effect and Anisotropic Scattering. *Icarus* 157, 523–534.
- Hapke, B., Dimucci, D., Nelson, R., Smythe, W., Mar. 1996. The Nature of the Opposition Effect in Frost, Vegetation and Soils. In: Lunar and Planetary Institute Conference Abstracts. Vol. 27 of Lunar and Planetary Inst. Technical Report. pp. 491–+.
- Harris, A. W., Young, J. W., Bowell, E., Martin, L. J., Millis, R. L., Poutanen, M., Scaltriti, F., Zappala, V., Schober, H. J., Debehogne, H., Zeigler, K. W., Jan. 1989a. Photoelectric observations of asteroids 3, 24, 60, 261, and 863. *Icarus* 77, 171–186.
- Harris, A. W., Young, J. W., Contreiras, L., Dockweiler, T., Belkora, L., Salo, H., Harris, W. D., Bowell, E., Poutanen, M., Binzel, R. P., Tholen, D. J., Wang, S., Oct. 1989b. Phase relations of high albedo asteroids - The unusual opposition brightening of 44 NYSA and 64 Angelina. *Icarus* 81, 365–374.
- Helfenstein, P., Veverka, J., Hillier, J., Jul. 1997. The Lunar Opposition Effect: A Test of Alternative Models. *Icarus* 128, 2–14.
- Ip, W.-H., May 1983. Collisional interactions of ring particles - The ballistic transport process. *Icarus* 54, 253–262.
- Irvine, W. M., 1966. The shadowing effect in diffuse reflection. *Journal of Geophysical Research* 71, 2931–2937.
- Kaasalainen, S., Oct. 2003. Laboratory photometry of planetary regolith analogs. I. Effects of grain and packing properties on opposition effect. *Astronomy and Astrophysics* 409, 765–769.
- Kaasalainen, S., Muinonen, K., Piironen, J., Aug. 2001. Comparative study

- on opposition effect of icy solar system objects. *Journal of Quantitative Spectroscopy and Radiative Transfer* 70, 529–543.
- Karkoschka, E., May 2001. Comprehensive Photometry of the Rings and 16 Satellites of Uranus with the Hubble Space Telescope. *Icarus* 151, 51–68.
- Kawata, Y., Irvine, W. M., 1974. Models of Saturn’s rings which satisfy the optical observations. In: Wozczyk, A., Iwaniszewska, C. (Eds.), *Exploration of the Planetary System*. Vol. 65 of IAU Symposium. pp. 441–464.
- Larson, S., 1984. Summary of Optical Ground-Based E Ring Observations at the University of Arizona. In: Greenberg, R., Brahic, A. (Eds.), *IAU Colloq. 75: Planetary Rings*. pp. 111–+.
- Lee, P., Helfenstein, P., Veverka, J., McCarthy, D., Sep. 1992. Anomalous-scattering region on Triton. *Icarus* 99, 82–97.
- Lissauer, J. J., Squyres, S. W., Hartmann, W. K., Nov. 1988. Bombardment history of the Saturn system. *Journal of Geophysical Research* 93, 13776–13804.
- Lockwood, G. W., Thompson, D. T., Lumme, K., Jul. 1980. A possible detection of solar variability from photometry of Io, Europa, Callisto, and Rhea, 1976-1979. *Astronomical Journal* 85, 961–968.
- Lumme, K., Irvine, W. M., Oct. 1976. Photometry of Saturn’s rings. *Astronomical Journal* 81, 865–893.
- Lumme, K., Peltoniemi, J., Irvine, W. M., 1990. Some photometric techniques for atmosphereless solar system bodies. *Advances in Space Research* 10, 187–193.
- McCord, T. B., Hansen, G. B., Hibbitts, C. A., May 2001. Hydrated Salt Minerals on Ganymede’s Surface: Evidence of an Ocean Below. *Science* 292, 1523–1525.
- McEwen, A. S., Soderblom, L. A., Johnson, T. V., Matson, D. L., Sep. 1988.

- The global distribution, abundance, and stability of SO₂ on Io. *Icarus* 75, 450–478.
- Millis, R. L., Thompson, D. T., Dec. 1975. UVB photometry of the Galilean satellites. *Icarus* 26, 408–419.
- Mishchenko, M. I., Aug. 1992. The angular width of the coherent back-scatter opposition effect - an application to icy outer planet satellites. *Astrophysics and Space Science* 194, 327–333.
- Mishchenko, M. I., Jul. 1993. On the nature of the polarization opposition effect exhibited by Saturn's rings. *Astrophysical Journal* 411, 351–361.
- Mishchenko, M. I., Dlugach, Z. M., Jan. 1992a. Can weak localization of photons explain the opposition effect of Saturn's rings? *Monthly Notices of the Royal Astronomical Society* 254, 15P–18P.
- Mishchenko, M. I., Dlugach, Z. M., Mar. 1992b. The amplitude of the opposition effect due to weak localization of photons in discrete disordered media. *Astrophysics and Space Science* 189, 151–154.
- Mishchenko, M. I., Rosenbush, V. K., N., K. N., 2006. Weak localization of electromagnetic waves and opposition phenomena exhibited by high-albedo atmosphereless solar system objects. *Applied Optics* 45, 4459–4463.
- Morrison, D., Morrison, N. D., Lazarewicz, A. R., Nov. 1974. Four-color photometry of the Galilean satellites. *Icarus* 23, 399–416.
- Muinonen, K., Zubko, E., Tyynelä, J., Shkuratov, Y. G., Videen, G., Jul. 2007. Light scattering by Gaussian random particles with discrete-dipole approximation. *Journal of Quantitative Spectroscopy and Radiative Transfer* 106, 360–377.
- Müller, G., 1885. Resultate aus Helligkeitsmessungen des Planeten Saturn. *Astronomische Nachrichten* 110, 225–+.
- Murray, C. D., Dermott, S. F., Feb. 2000. *Solar System Dynamics*. Solar Sys-

- tem Dynamics, ISBN 0521575974, UK: Cambridge University Press, 2000.
- Nelson, R. M., Hapke, B. W., Smythe, W. D., Spilker, L. J., Oct. 2000. The Opposition Effect in Simulated Planetary Regoliths. Reflectance and Circular Polarization Ratio Change at Small Phase Angle. *Icarus* 147, 545–558.
- Neukum, G., Ivanov, B. A., Hartmann, W. K., Apr. 2001. Cratering Records in the Inner Solar System in Relation to the Lunar Reference System. *Space Science Reviews* 96, 55–86.
- Pang, K. D., Voge, C. C., Rhoads, J. W., Ajello, J. M., Mar. 1983. Saturn's E-Ring and Satellite Enceladus. In: Lunar and Planetary Institute Conference Abstracts. Vol. 14 of Lunar and Planetary Inst. Technical Report. pp. 592–593.
- Pappalardo, R. T., Head, J. W., Collins, G. C., Kirk, R. L., Neukum, G., Oberst, J., Giese, B., Greeley, R., Chapman, C. R., Helfenstein, P., Moore, J. M., McEwen, A., Tufts, B. R., Senske, D. A., Breneman, H. H., Klaasen, K., Sep. 1998a. Grooved Terrain on Ganymede: First Results from Galileo High-Resolution Imaging. *Icarus* 135, 276–302.
- Pappalardo, R. T., Head, J. W., Greeley, R., Sullivan, R. J., Pilcher, C., Schubert, G., Moore, W. B., Carr, M. H., Moore, J. M., Belton, M. J. S., Goldsby, D. L., Jan. 1998b. Geological evidence for solid-state convection in Europa's ice shell. *Nature* 391, 365–+.
- Pierce, A. K., Waddell, J. H., 1961. Analysis of Limb Darkening Observations. *Memoirs Royal Astron. Soc.* 63, 89–112.
- Porco, C. C., Aug. 1991. An explanation for Neptune's ring arcs. *Science* 253, 995–1001.
- Porco, C. C., Helfenstein, P., Thomas, P. C., Ingersoll, A. P., Wisdom, J., West, R., Neukum, G., Denk, T., Wagner, R., Roatsch, T., Kieffer, S., Turtle, E., McEwen, A., Johnson, T. V., Rathbun, J., Veverka, J., Wilson, D., Perry,

- J., Spitale, J., Brahic, A., Burns, J. A., DelGenio, A. D., Dones, L., Murray, C. D., Squyres, S., Mar. 2006. Cassini Observes the Active South Pole of Enceladus. *Science* 311, 1393–1401.
- Poulet, F., Cuzzi, J. N., French, R. G., Dones, L., Jul. 2002. A Study of Saturn’s Ring Phase Curves from HST Observations. *Icarus* 158, 224–248.
- Rougier, G., 1933. Photometrie photoelectrique globale de la lune. *Annales de l’Observatoire de Strasbourg* 2, 203–+.
- Rozenbush, V., Kiselev, N., Avramchuk, V., Mishchenko, M. 2002. Photometric and polarimetric opposition phenomena exhibited by solar system bodies, In Videen, G., Kocifaj, M. (Eds.) *Optics of Cosmic Dust*, Kluwer Academic Publisher. Dordrecht, Netherlands, pp. 191-224.
- Schaefer, B. E., Tourtellotte, S. W., May 2001. Photometric Light Curve for Nereid in 1998: A Prominent Opposition Surge. *Icarus* 151, 112–117.
- Seeliger, H., 1884. Zur Photometrie des Saturnringes. *Astronomische Nachrichten* 109, 305–+.
- Shkuratov, I. G., Feb. 1991. The effect of the finiteness of the angular dimensions of a light source on the magnitude of the opposition effect of the luminosity of atmosphereless bodies. *Astronomicheskii Vestnik* 25, 71–75.
- Shkuratov, Y. G., Kreslavsky, M. A., Ovcharenko, A. A., Stankevich, D. G., Zubko, E. S., Pieters, C., Arnold, G., Sep. 1999. Opposition Effect from Clementine Data and Mechanisms of Backscatter. *Icarus* 141, 132–155.
- Showalter, M. R., Burns, J. A., Cuzzi, J. N., Pollack, J. B., Mar. 1987. Jupiter’s ring system - New results on structure and particle properties. *Icarus* 69, 458–498.
- Showalter, M. R., Cuzzi, J. N., Larson, S. M., Dec. 1991. Structure and particle properties of Saturn’s E Ring. *Icarus* 94, 451–473.
- Simonelli, D. P., Kay, J., Adinolfi, D., Veverka, J., Thomas, P. C., Helfenstein,

- P., Apr. 1999. Phoebe: Albedo Map and Photometric Properties. *Icarus* 138, 249–258.
- Smith, B. A., Soderblom, L., Beebe, R. F., Boyce, J. M., Briggs, G., Bunker, A., Collins, S. A., Hansen, C., Johnson, T. V., Mitchell, J. L., Terrile, R. J., Carr, M. H., Cook, A. F., Cuzzi, J. N., Pollack, J. B., Danielson, G. E., Ingersoll, A. P., Davies, M. E., Hunt, G. E., Masursky, H., Shoemaker, E. M., Morrison, D., Owen, T., Sagan, C., Veverka, J., Strom, R., Suomi, V. E., Apr. 1981. Encounter with Saturn - Voyager 1 imaging science results. *Science* 212, 163–191.
- Spitale, J. N., Jacobson, R. A., Porco, C. C., Owen, Jr., W. M., Aug. 2006. The Orbits of Saturn's Small Satellites Derived from Combined Historic and Cassini Imaging Observations. *The Astronomical Journal* 132, 692–710.
- Squyres, S. W., Veverka, J., May 1981. Voyager photometry of surface features on Ganymede and Callisto. *Icarus* 46, 137–155.
- Stankevich, D. G., Shkuratov, Y. G., Muimonen, K., 1999. Shadow hiding effect in inhomogeneous layered particulate media. *J. Quant. Spectrosc. Radiat. Transfer* 63, 445–448.
- Sullivan, R., Greeley, R., Homan, K., Klemaszewski, J., Belton, M. J. S., Carr, M. H., Chapman, C. R., Tufts, R., Head, J. W., Pappalardo, R., Moore, J., Thomas, P., Jan. 1998. Episodic plate separation and fracture infill on the surface of Europa. *Nature* 391, 371–+.
- Thomas, P., Veverka, J., Helfenstein, P., Oct. 1991. Voyager observations of Nereid. *Journal of Geophysical Research* 96, 19253–+.
- Thompson, D. T., Lockwood, G. W., Sep. 1992. Photoelectric photometry of Europa and Callisto 1976-1991. *Journal of Geophysical Research* 97, 14761–+.
- Throop, H. B., Porco, C. C., West, R. A., Burns, J. A., Showalter, M. R.,

- Nicholson, P. D., Nov. 2004. The jovian rings: new results derived from Cassini, Galileo, Voyager, and Earth-based observations. *Icarus* 172, 59–77.
- Verbiscer, A., French, R., Showalter, M., Helfenstein, P., Feb. 2007. Enceladus: Cosmic Graffiti Artist Caught in the Act. *Science* 315, 815–.
- Verbiscer, A., Veverka, J., Jun. 1991. Detection of Albedo Markings on Enceladus. In: *Bulletin of the American Astronomical Society*. Vol. 23 of *Bulletin of the American Astronomical Society*. pp. 1168–+.
- Verbiscer, A. J., French, R. G., McGhee, C. A., Jan. 2005. The opposition surge of Enceladus: HST observations 338-1022 nm. *Icarus* 173, 66–83.
- Verbiscer, A. J., Veverka, J., Dec. 1989. Albedo dichotomy of RHEA - Hapke analysis of Voyager photometry. *Icarus* 82, 336–353.
- Verbiscer, A. J., Veverka, J., Dec. 1990. Scattering properties of natural snow and frost - Comparison with icy satellite photometry. *Icarus* 88, 418–428.
- Veverka, J., Thomas, P., Helfenstein, P., Brown, R. H., Johnson, T. V., Dec. 1987. Satellites of Uranus - Disk-integrated photometry from Voyager imaging observations. *Journal of Geophysical Research* 92, 14895–14904.
- Whitaker, E. A., 1969. An Investigation of the Lunar Heiligenschein. NASA Special Publication 201, 38–+.
- Wisdom, J., Tremaine, S., Mar. 1988. Local simulations of planetary rings. *Astronomical Journal* 95, 925–940.
- Zahnle, K., Schenk, P., Levison, H., Dones, L., Jun. 2003. Cratering rates in the outer Solar System. *Icarus* 163, 263–289.

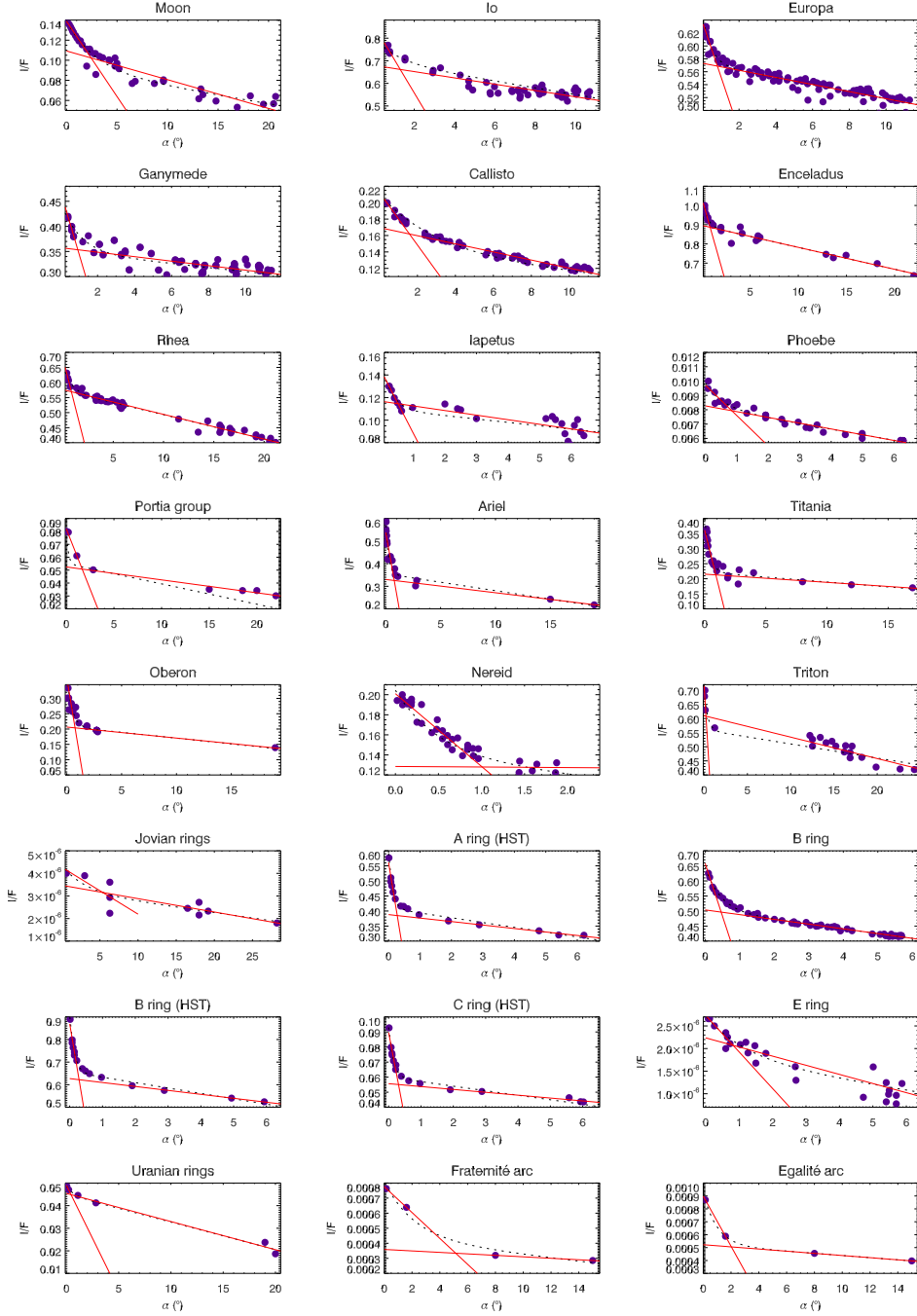


Fig. 1. Phase curves of a selection of rings and satellites in the Solar System (see Table 1 for references). The solid curves correspond to the best fit obtained with the linear-by-parts model and the dotted curves to the best linear-exponential fit.

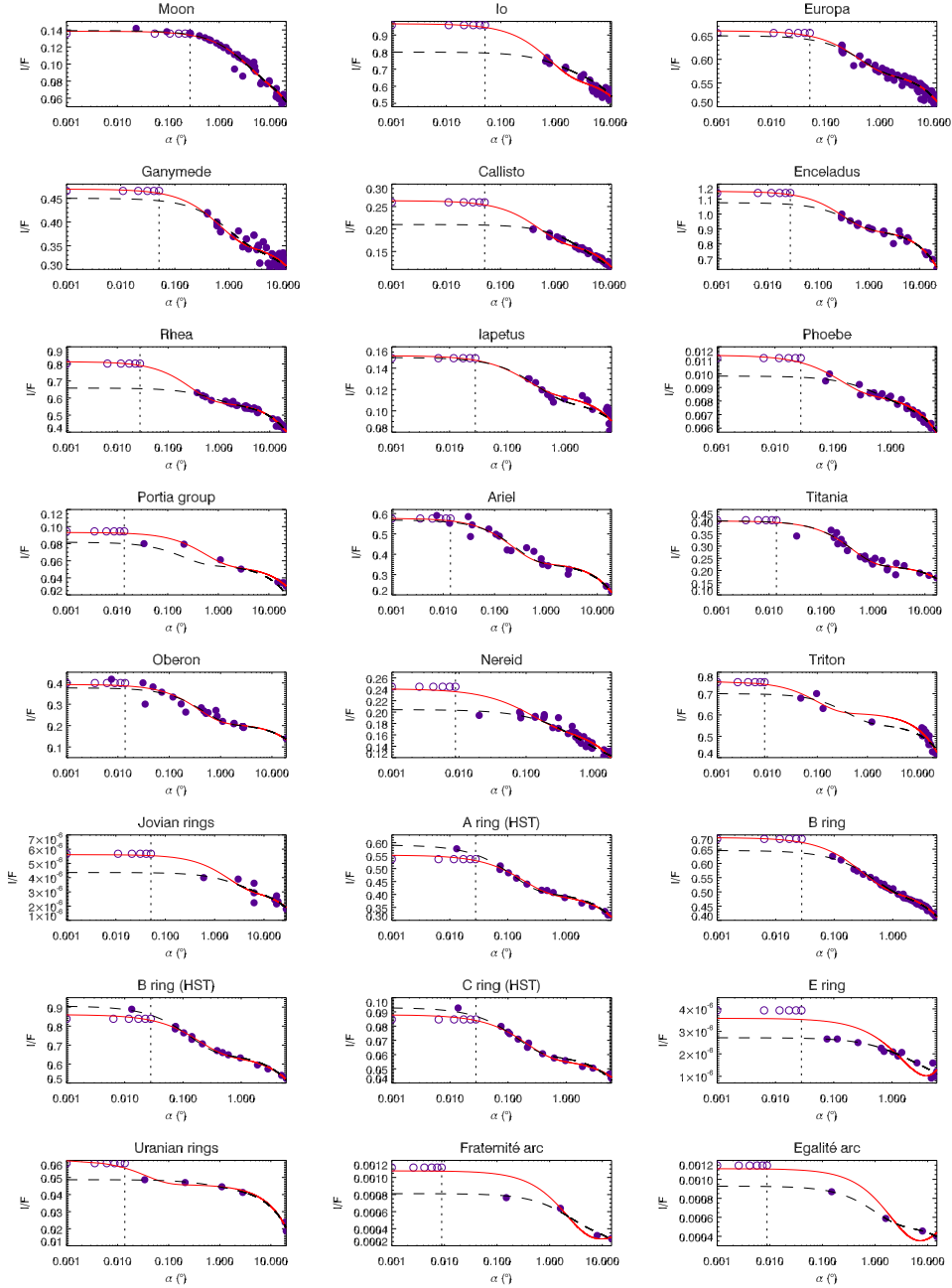


Fig. 2. Phase curves of a selection of rings and satellites in the Solar System. The solid curves correspond to the best fit obtained with the linear-exponential model convolved with the size of the Sun (using extrapolated data below the angular size of the Sun, empty symbols) and the dashed curves correspond to the best linear-exponential fit (using only original data, filled symbols). The vertical dotted lines represent the angular size of the Sun at the observation time (see Table 6 of Appendix).

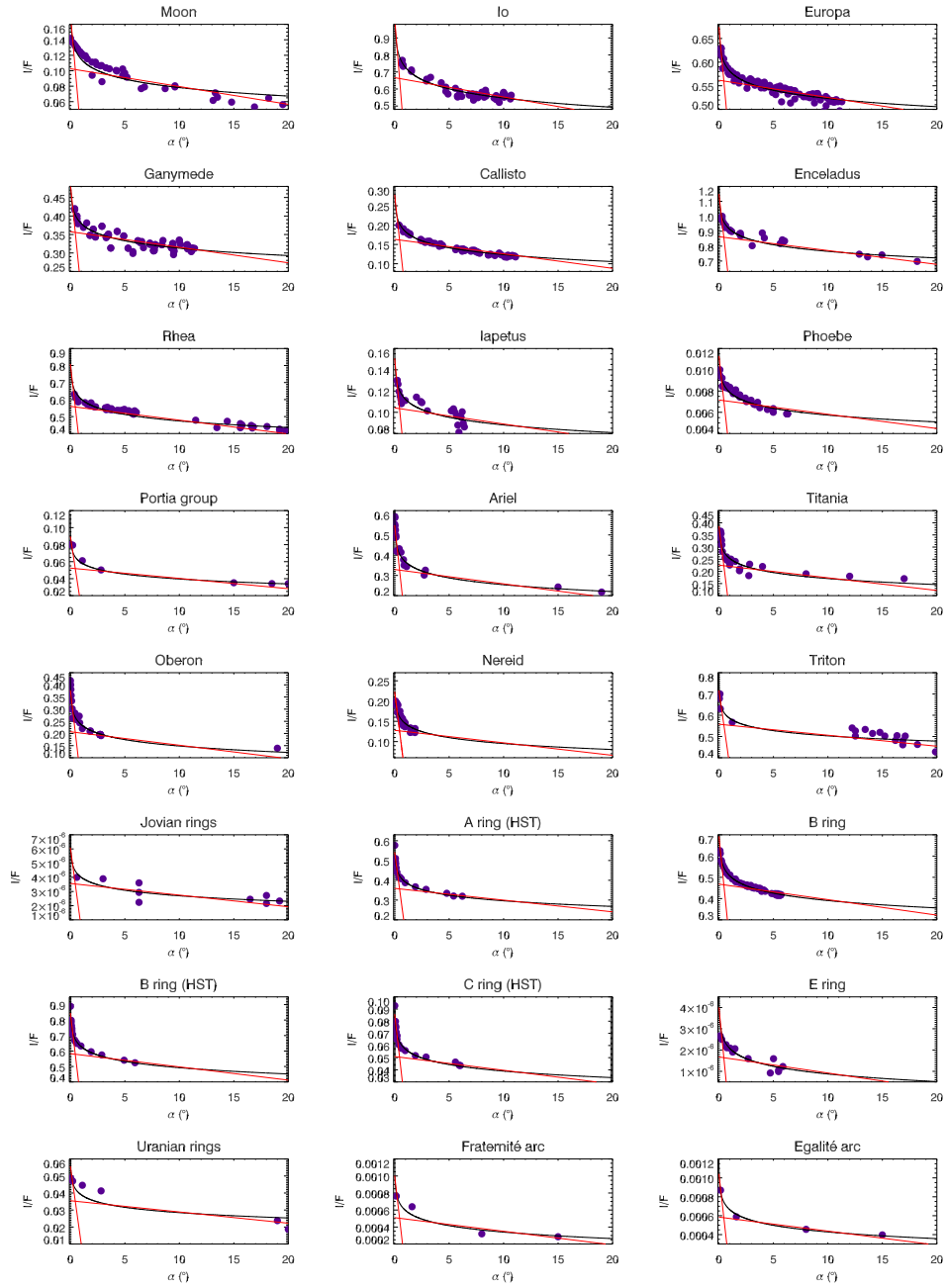


Fig. 3. Phase curves of a selection of rings and satellites in the Solar System. The solid lines correspond to the best fit obtained with the linear-by-parts fit to the logarithmic model (in solid curves).

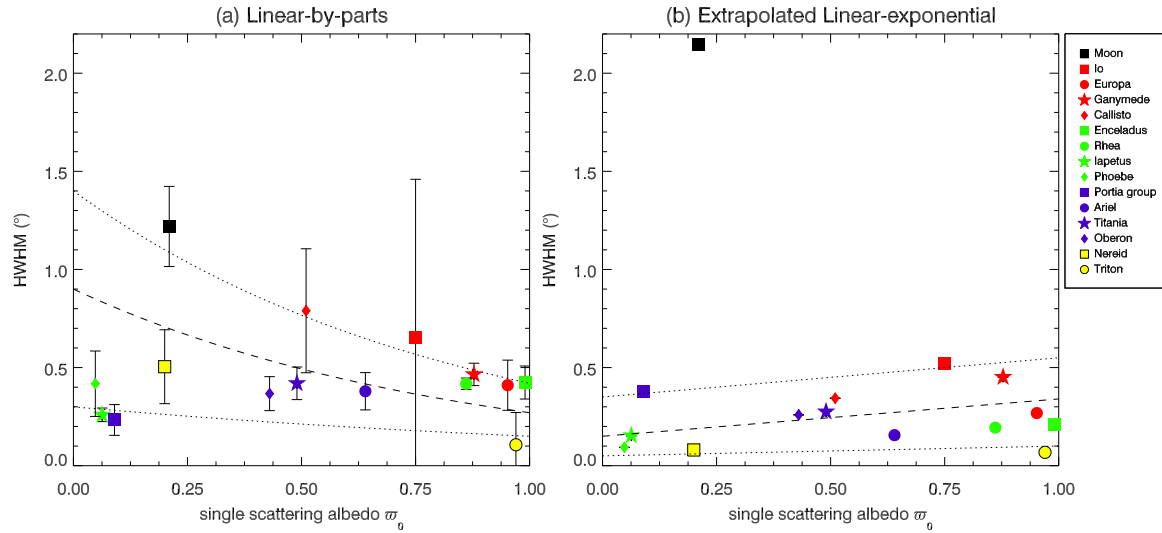


Fig. 4. HWHM of the surge for satellites of Jupiter, Saturn, Uranus and Neptune derived with : (a) the linear-by-parts model and (b) the linear-exponential model convolved with the size of the Sun.

In (a) dashed line corresponds to a power-law fit to the data which is $\text{HWHM} \sim 0.9 \times 0.3^{\varpi_0}$.

In (b) dashed line corresponds to a linear fit $\text{HWHM} \sim 0.15 + 0.19\varpi_0$.

Dotted lines are empirical functions to the boundaries of the data.

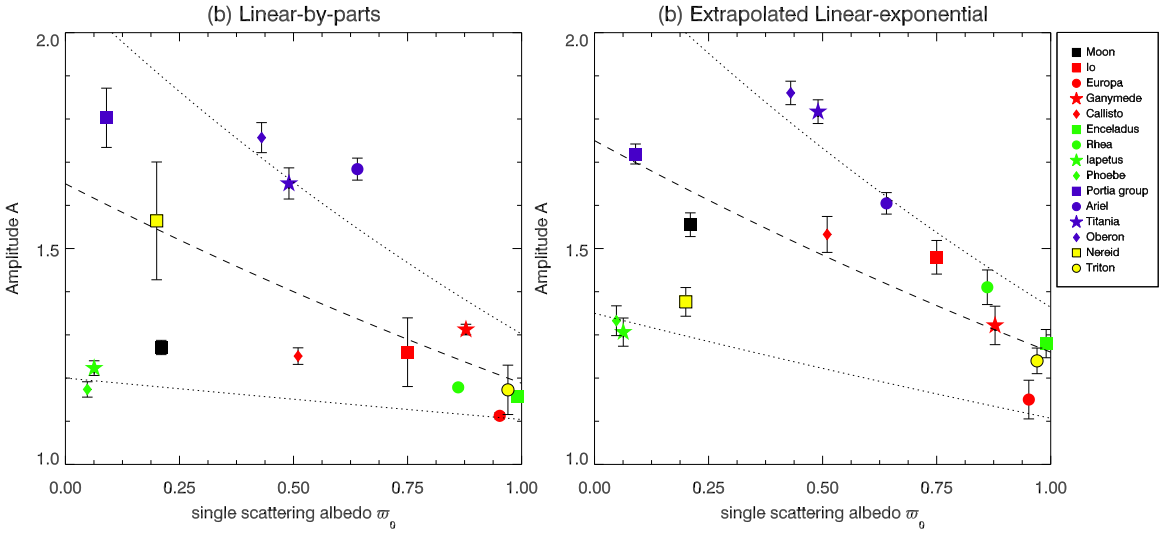


Fig. 5. Amplitude of the surge derived with the linear-by-parts model for satellites of Jupiter, Saturn, Uranus and Neptune : (a) the linear-by-parts model and (b) the linear-exponential model convolved with the size of the Sun.

In (a) dashed line corresponds to a power fit to the data $A \sim 1.65 \times 0.72^{\varpi_0}$

In (b) dashed line corresponds to the fit $A \sim 1.75 \times 0.72^{\varpi_0}$.

Dotted lines are empirical functions to the data boundaries.

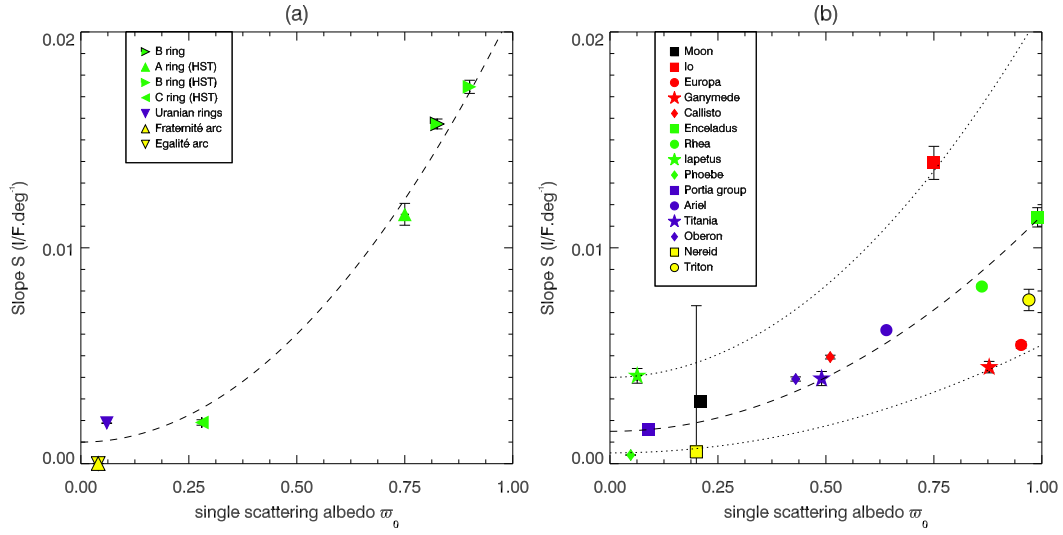


Fig. 6. Morphological parameter S derived with the linear-by-parts model for : rings (a) and satellites (b) of Jupiter, Saturn, Uranus and Neptune.

In (a) dashed line corresponds to a power-law fit to the data which is $S \sim 0.001 + 0.02\sigma_0^2$

In (b) dashed line corresponds to a fit to the data which is $S \sim 0.001 + 0.01\sigma_0^2$.

Dotted lines are empirical functions to the data boundaries.

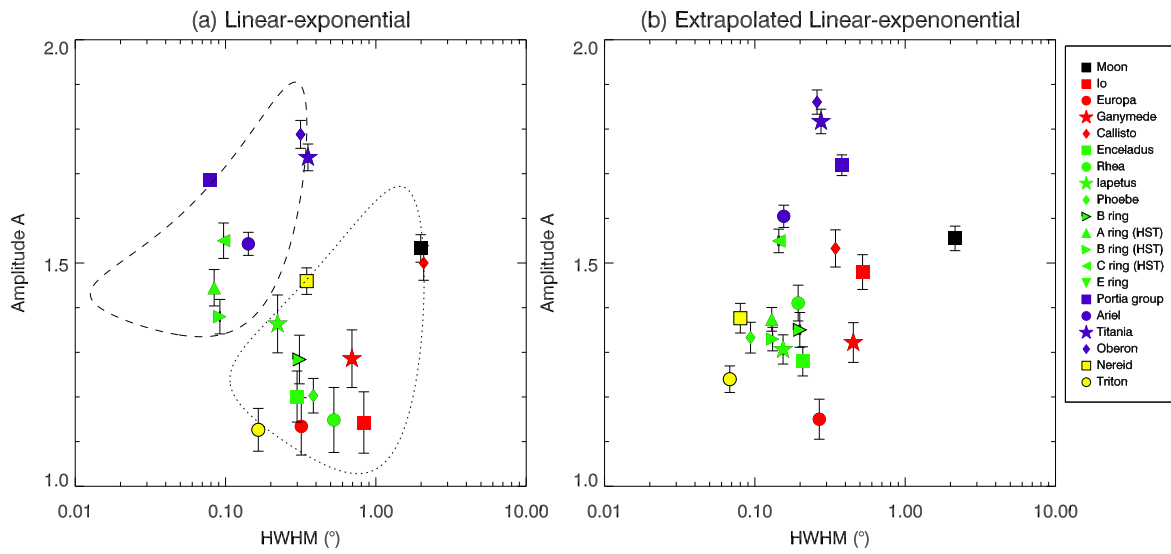


Fig. 7. Cross comparison between the morphological parameters of the surge derived (a) with the linear-exponential model and (b) with the linear-exponential model convolved with the size of the Sun (see tables 7 and 6 of Appendix).

Dashed and dotted ellipses are arbitrary delimitations of the data points (see text).

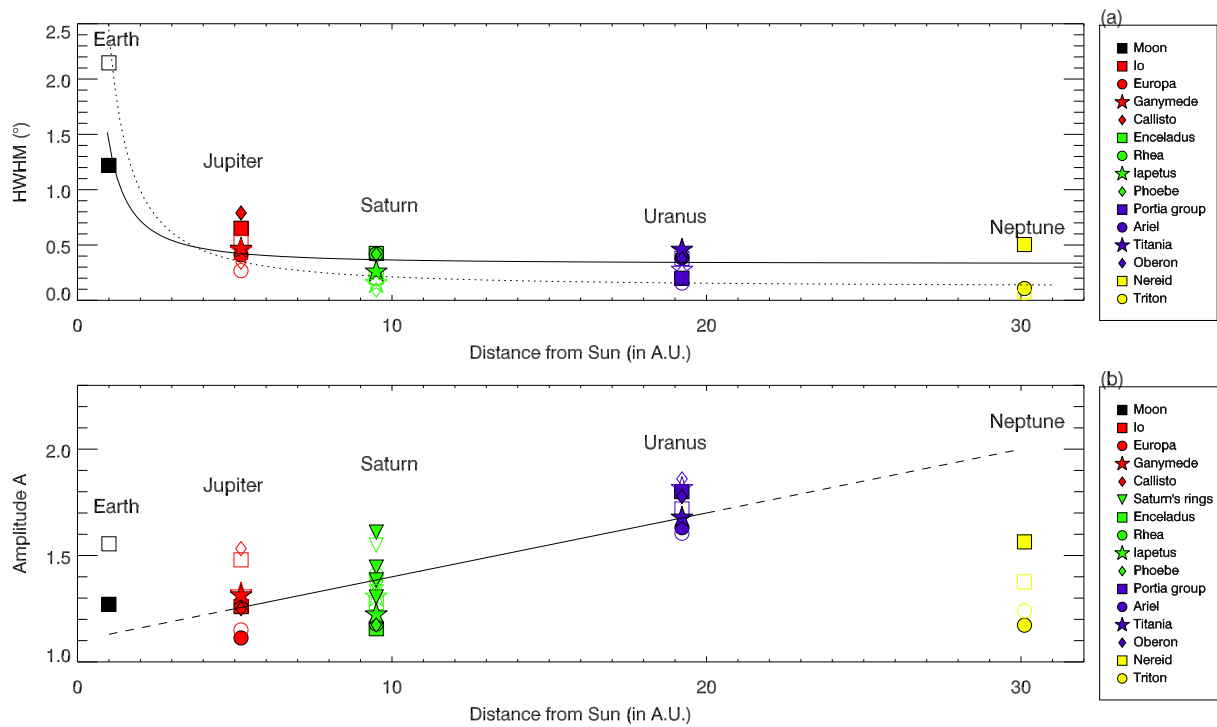


Fig. 8. Variation of the morphological parameters HWHM and A derived with the linear-by-parts model (filled symbols and solid line) and the extrapolated linear-exponential model (empty symbols and dotted line) with respect to the distance from the Sun (distances are taken from Murray and Dermott, 2000).

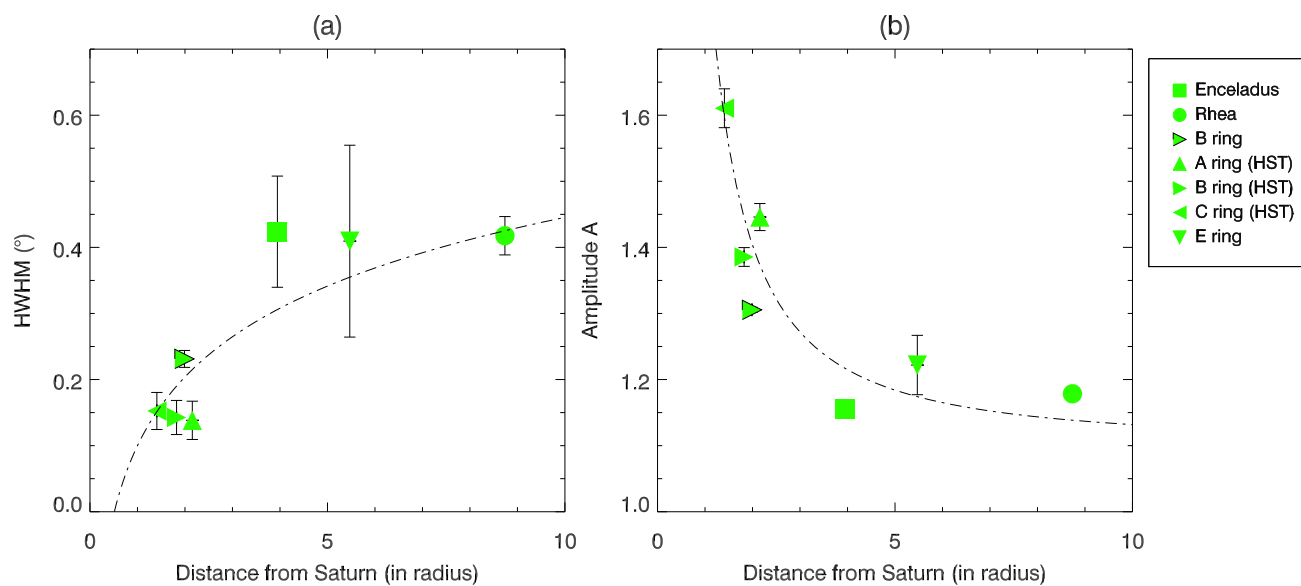


Fig. 9. Variation of the morphological parameters: the amplitude A of the surge (a) and the half-width at half-maximum HWHM (b) derived with the linear-by-parts model with the distance from Saturn.

(Distances are taken from Murray and Dermott, 2000).

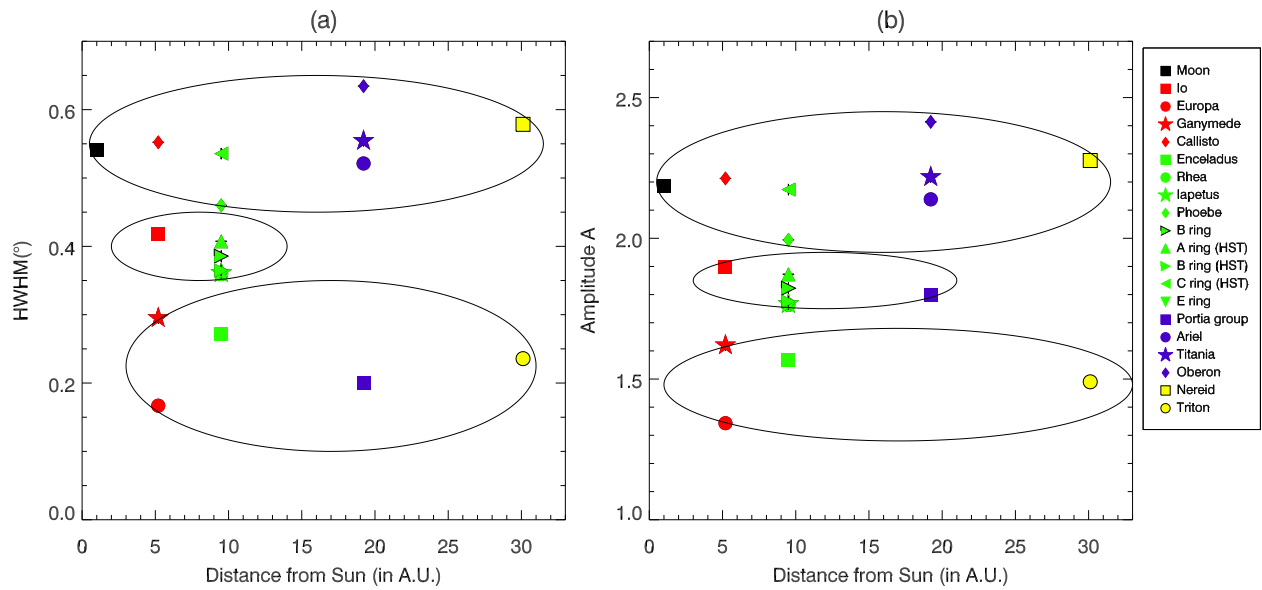


Fig. 10. Variation of the morphological parameters: the amplitude A of the surge (a) and the half-width at half-maximum HWHM (b) derived with the logarithmic model fitted by the linear-by-parts model with the distance from Saturn.

(Distances are taken from Murray and Dermott, 2000).

Solid ellipses in (a) and (b) are arbitrary delimitations of the data points (see text).

Table 1

References for opposition phase curves of the selection of Solar System rings and satellites.

	Object	λ (nm)	References
	Moon	~ 570	(Whitaker, 1969; Rougier, 1933)
Jupiter	Main ring	~ 460	(Throop et al., 2004)
	Io	~ 570	(McEwen et al., 1988)
	Europa	~ 500	(Thompson and Lockwood, 1992)
	Ganymede	~ 600	(Morrison et al., 1974; Millis and Thompson, 1975; Blanco and Catalano, 1974)
	Callisto	~ 500	(Thompson and Lockwood, 1992)
		C ring	672
Saturn	B ring	~ 650	(Franklin and Cook, 1965)
	B ring (HST)	672	(French et al., 2007)
	A ring	672	(French et al., 2007)
	E ring	~ 650	(Pang et al., 1983; Larson, 1984; Showalter et al., 1991)
	Enceladus	439	(Verbiscer et al., 2005)
	Rhea	~ 500	(Domingue et al., 1995; Verbiscer and Veverka, 1989)
	Iapetus	~ 600	(Franklin and Cook, 1974)
	Phoebe	~ 650	(Bauer et al., 2006)
Uranus	Rings	~ 500	(Karkoschka, 2001)
	Portia <i>group</i>	~ 500	(Karkoschka, 2001)
	Ariel	~ 600	(Buratti et al., 1992; Karkoschka, 2001)
	Titania	~ 600	(Buratti et al., 1992; Karkoschka, 2001)
	Oberon	~ 600	(Buratti et al., 1992; Karkoschka, 2001)
Neptune	Fraternité	~ 500	(de Pater et al., 2005; Ferrari and Brahic, 1994)
	Egalité	~ 500	(de Pater et al., 2005; Ferrari and Brahic, 1994)
	Nereid	~ 570	(Schaefer and Tourtellotte, 2001)
	Triton	~ 400	(Buratti et al., 1991)

Table 2

Morphological parameters of opposition phase curves of Solar System objects. The unit of HWHM is the degree and the unit of the slope S is I/F.deg⁻¹

Object	Linear-by-parts fit			Linear-exponential fit			
	A	HWHM	S	A	HWHM	S	
Moon	1.27	1.21	0.0261	1.53	1.98	0.0017	
Jupiter	Main ring	1.23	2.68	0.0170	1.34	2.03	4.82×10^{-8}
	Io	1.25	0.65	0.0204	1.14	0.83	0.01500
	Europa	1.11	0.41	0.0095	1.13	0.31	0.0054
	Ganymede	1.31	0.46	0.0125	1.28	0.69	0.0040
	Callisto	1.25	0.78	0.0291	1.50	2.07	0.0024
Saturn	C ring	1.61	0.15	0.0342	1.55	0.09	0.0030
	B ring	1.30	0.23	0.0312	1.28	0.30	0.0155
	B ring (HST)	1.38	0.14	0.0278	1.37	0.09	0.0238
	A ring	1.44	0.13	0.0297	1.44	0.08	0.0159
	E ring	1.22	0.40	0.0903	1.51	0.86	1.19×10^{-7}
	Enceladus	1.15	0.42	0.0127	1.20	0.29	0.0113
	Rhea	1.17	0.41	0.0142	1.14	0.52	0.0080
	Iapetus	1.22	0.25	0.0348	1.36	0.22	0.0030
	Phoebe	1.17	0.41	0.0485	1.20	0.38	0.0003
Uranus	Rings	1.07	0.21	0.0274	1.08	0.45	0.0012
	Portia <i>group</i>	1.80	0.20	0.0015	1.48	0.13	0.0015
	Ariel	1.63	0.38	0.0178	1.60	0.18	0.0074
	Titania	1.67	0.45	0.0126	1.82	0.27	0.0032
	Oberon	1.77	0.37	0.0174	1.81	0.31	0.0037
Neptune	Fraternité	2.16	2.57	0.0136	1.86	1.50	1.10×10^{-5}
	Egalité	1.72	1.01	0.0160	1.77	0.67	8.34×10^{-6}
	Nereid	1.56	0.50	0.0042	1.45	0.34	0.0099
	Triton	1.17	0.10	0.0124	1.25	0.27	0.0049

Table 3

Direct output parameters of morphological models using opposition phase curves and “ideal” opposition phase curves of Solar System objects. The unit of w is the degree and the unit of the slope I_s is I/F.deg⁻¹

Object	Logarithmic fit		Linear-exponential fit				Extrapolated linear-exponential fit				
	a_0	a_1	I_p	I_b	w	I_s	I_p	I_b	w	I_s	
Moon	0.114	-0.015	0.048	0.090	1.433	0.0017	0.049	0.088	1.548	0.0016	
Main ring	3.9×10^{-6}	-5.6×10^{-7}	1.1×10^{-6}	3.2×10^{-6}	1.470	4.8×10^{-8}	2.4×10^{-6}	3.2×10^{-6}	0.905	4.6×10^{-8}	
Jupiter	Io	0.726	-0.077	0.100	0.699	0.600	0.0150	0.313	0.652	0.375	0.0107
	Europa	0.580	-0.025	0.076	0.572	0.230	0.0054	0.086	0.573	0.193	0.0055
	Ganymede	0.379	-0.028	0.100	0.349	0.500	0.0040	0.114	0.355	0.325	0.0041
	Callisto	0.182	-0.025	0.070	0.140	1.500	0.0024	0.091	0.171	0.248	0.0051
	C ring	0.056	-0.007	0.033	0.059	0.070	0.0030	0.031	0.056	0.104	0.0021
Saturn	B ring	0.506	-0.050	0.142	0.502	0.223	0.0155	0.179	0.511	0.143	0.0174
	B ring (HST)	0.628	-0.058	0.249	0.656	0.066	0.0238	0.213	0.647	0.094	0.0216
	A ring	0.390	-0.046	0.182	0.409	0.060	0.0159	0.150	0.401	0.093	0.0143
	E ring	2.1×10^{-6}	-5.2×10^{-7}	9.3×10^{-7}	1.8×10^{-6}	0.623	1.2×10^{-7}	4.8×10^{-7}	1.2×10^{-6}	1.085	3.8×10^{-7}
	Enceladus	0.912	-0.063	0.180	0.895	0.215	0.0113	0.251	0.899	0.150	0.0116
	Rhea	0.602	-0.055	0.085	0.573	0.379	0.0080	0.236	0.576	0.139	0.0082
	Iapetus	0.112	-0.010	0.039	0.110	0.160	0.0030	0.035	0.116	0.111	0.0039
	Phoebe	0.007	-0.0001	0.001	0.008	0.276	0.0003	0.002	0.008	0.067	0.0004
	Rings	0.038	-0.004	0.003	0.044	0.326	0.0012	0.014	0.045	0.017	0.0012
Uranus	Portia group	0.058	-0.006	0.026	0.055	0.100	0.0015	0.038	0.054	0.273	0.0010
	Ariel	0.366	-0.044	0.213	0.355	0.129	0.0074	0.217	0.359	0.112	0.0077
	Titania	0.252	-0.034	0.181	0.221	0.198	0.0032	0.181	0.221	0.198	0.0032
	Oberon	0.236	-0.034	0.168	0.208	0.229	0.0037	0.181	0.211	0.186	0.0040
	Rings	0.038	-0.004	0.003	0.044	0.326	0.0012	0.014	0.045	0.017	0.0012
Neptune	Fraternité	0.0005	-0.0001	0.00037	0.00043	1.082	1.1×10^{-5}	0.00086	0.00022	1.1×10^{-5}	5.6×10^{-6}
	Egalité	0.0001	-0.001	0.00040	0.00052	0.489	8.3×10^{-6}	0.00090	0.00021	1.106	1.5×10^{-5}
	Nereid	0.144	-0.021	0.064	0.140	0.250	0.0099	0.065	0.175	0.057	0.0301
	Triton	0.584	-0.035	0.140	0.560	0.200	0.0049	0.146	0.609	0.049	0.0075

Table 4

References for the single scattering albedo of Solar System objects.

	Object	ϖ_0	λ (nm)	References
	Moon	0,21	~ 500	(Helfenstein et al., 1997)
Jupiter	Io	0,75	590	(McEwen et al., 1988)
	Europa	0,96	550	(Domingue and Verbiscer, 1997)
	Ganymede	0,87	470	(Domingue and Verbiscer, 1997)
	Callisto	0,53	470	(Domingue and Verbiscer, 1997)
Saturn	C ring	0,16	672	(French et al., 2007)
	B ring	0,83	672	(Poulet et al., 2002)
	B ring (HST)	0,85	672	(French et al., 2007)
	A ring	0,79	672	(French et al., 2007)
	Enceladus	0,99	480	(Verbiscer and Veverka, 1991)
	Rhea	0,86	480	(Verbiscer and Veverka, 1989)
	Iapetus	0,16	480	(Buratti, 1984)
	Phoebe	0,06	480	(Simonelli et al., 1999)
Uranus	Rings	0,06	~ 500	(Karkoschka, 2001)
	Portia <i>group</i>	0,09	~ 500	(Karkoschka, 2001)
	Ariel	0,64	~ 500	(Karkoschka, 2001)
	Titania	0,48	~ 475	(Veverka et al., 1987)
	Oberon	0,43	~ 500	(Karkoschka, 2001)
Neptune	Fraternité	0,02	480	(Ferrari and Brahic, 1994)
	Egalité	0,02	480	(Ferrari and Brahic, 1994)
	Nereid	0,21	~ 500	(Thomas et al., 1991)
	Triton	0,97	500	(Lee et al., 1992)

Table 5

Morphological parameters of “ideal” opposition phase curves of Solar System objects. The unit of HWHM is the degree and the unit of the slope S is $I/F.\text{deg}^{-1}$

Object	Linear-by-parts and log fits			Extrapolated linear-exponential fit			
	A	HWHM	S	A	HWHM	S	
Moon	2.18	0.54	0.0224	1.55	2.14	0.0016	
Jupiter	Main ring	2.21	0.55	0.0230	1.76	1.25	4.55×10^{-8}
	Io	1.89	0.41	0.0169	1.47	0.52	0.0107
	Europa	1.34	0.16	0.0064	1.15	0.26	0.0055
	Ganymede	1.62	0.29	0.0117	1.32	0.45	0.0041
	Callisto	2.21	0.55	0.0229	1.53	0.34	0.0051
Saturn	C ring	2.17	0.53	0.0221	1.54	0.14	0.0021
	B ring	1.82	0.38	0.0155	1.35	0.19	0.0174
	B ring (HST)	1.77	0.36	0.0146	1.32	0.13	0.0216
	A ring	1.87	0.40	0.0165	1.37	0.12	0.0143
	E ring	3.38	0.99	0.0450	2.80	1.50	3.76×10^{-7}
	Enceladus	1.56	0.27	0.0107	1.27	0.20	0.0116
	Rhea	1.76	0.35	0.0144	1.41	0.19	0.0082
	Iapetus	1.76	0.36	0.0145	1.30	0.15	0.0039
	Phoebe	1.99	0.45	0.0187	1.33	0.09	0.0004
Uranus	Rings	1.98	0.45	0.0186	1.31	0.02	0.0012
	Portia <i>group</i>	1.80	0.20	0.0015	1.71	0.37	0.0010
	Ariel	2.13	0.52	0.0215	1.60	0.15	0.0077
	Titania	2.21	0.55	0.0230	1.81	0.27	0.0032
	Oberon	2.41	0.63	0.0267	1.86	0.25	0.0040
Neptune	Fraternité	2.72	0.75	0.0314	4.99	1.53	5.61×10^{-6}
	Egalité	2.39	0.62	0.0253	5.34	1.53	1.53×10^{-5}
	Nereid	2.27	0.57	0.0241	1.37	0.08	0.0301
	Triton	1.49	0.23	0.0092	1.23	0.06	0.0075

APPENDIX :

REFINEMENTS TO THE SUN’S ANGULAR SIZE EFFECT To compute the distance from a Solar System object to the Sun at any given date, it is not appropriate to use the semi-major axis. We use a series of equations which take into consideration the distance between the Sun and the planet at the approximate date. The heliocentric radius r_p , the distance from the focus of the ellipse (i.e. the Sun) to the planet, is given by:

$$r_p = a(1 - e \cos E) \quad (10)$$

where E is the eccentric anomaly, a and e are two of the seven orbital elements which define an ellipse in space : a is the mean distance, or the value of the semi-major axis of the orbit (average Sun to planet distance); e is the eccentricity of the ellipse which describes the orbit (dimensionless); i is the inclination (in degrees), or angle between the plane of the ecliptic (the plane of the Earth’s orbit about the Sun) and the plane of the planets orbit; Ω is the longitude of ascending node (in degrees), or the position in the orbit where the elliptical path of the planet passes through the plane of the ecliptic, from below the plane to above the plane; $\tilde{\omega}$ is the longitude of perihelion (in degrees), or the position in the orbit where the planet is closest to the Sun; λ is the mean longitude (in degrees), the position of the planet in the orbit; and M is mean anomaly (in degrees). The mean anomaly gives the planet’s angular position for a circular orbit with radius equal to the semi major axis. It is computed directly from the elements using:

$$M = \lambda - \tilde{\omega} \quad (11)$$

Kepler’s second law states that the radius vector of a planet sweeps out equal areas in equal times. The planet must speed up and slow down in its orbit. The true anomaly f gives the planet’s actual angular position in its orbit. It is the angle (at the Sun) between perihelion of the orbit and the current location of the planet. To obtain its value, first we compute the eccentric anomaly, E , from M and the eccentricity e by using the “Kepler equation”:

$$M = E - e \sin E \quad (12)$$

An expansion to order e^3 of the solution to the ‘‘Kepler equation’’ is:

$$E = M + \left(e - \frac{e^3}{8}\right) \sin M + \frac{1}{2}e^2 \sin 2M + \frac{3}{8}e^3 \sin 3M \quad (13)$$

Now, to find the orbital elements of a planet at a specific date, we use:

$$a = a_0 + \dot{a}t \quad (14)$$

$$e = e_0 + \dot{e}t \quad (15)$$

$$i = i_0 + (\dot{i}/3600) t \quad (16)$$

$$\tilde{\omega} = \tilde{\omega}_0 + (\dot{\tilde{\omega}}/3600) t \quad (17)$$

$$\Omega = \Omega_0 + (\dot{\Omega}/3600) t \quad (18)$$

$$\lambda = \lambda_0 + \left(\dot{\lambda}/3600 + 360 N_r\right) t \quad (19)$$

where t is the observation time (Table Appendix6) converted in Julian centuries since JD 2451545.0, the zero index quantities are the orbital elements at the epoch of J2000 (JD 2451545.0) and the dot quantities are the change per julian century of the orbital elements (values are taken in Murray and Dermott, 2000). When we have the heliocentric radius at the given observation time, we can compute the solar angular size α_\odot using r_p and r_\odot , the radius of the Sun:

$$\alpha_\odot = \arcsin \frac{r_\odot}{r_p} \quad (20)$$

The limb darkening function of Pierce and Waddell (1961) has been used in the past to be convolved with a theoretical opposition effect function (Kawata and Irvine, 1974). Its formula is:

$$W(\mu') = a_\lambda + b_\lambda \mu' + c_\lambda \left[1 - \mu' \cdot \log \left(1 + \frac{1}{\mu'} \right) \right] \quad (21)$$

where $\mu' = \cos \theta'$ and θ' varies from 0 to the Sun’s angular radius α_\odot . a_λ , b_λ and c_λ are coefficients that depend on the wavelength (values are given in table Appendix7).

We perform a normalized convolution of the limb darkening function to the linear-exponential function $P(\alpha)$ by doing:

$$P'(\alpha) = \frac{\int_0^{\alpha_\odot} P(\alpha) \cdot W(\cos \theta') d\theta'}{\int_0^{\alpha_\odot} W(\cos \theta') d\theta'} \quad (22)$$

Table 6

References for the observational parameters needed to compute the angular size of the Sun α_{\odot} . Bold text corresponds to missing data replaced arbitrarily, we assumed an hourly time of 18:00:00.0

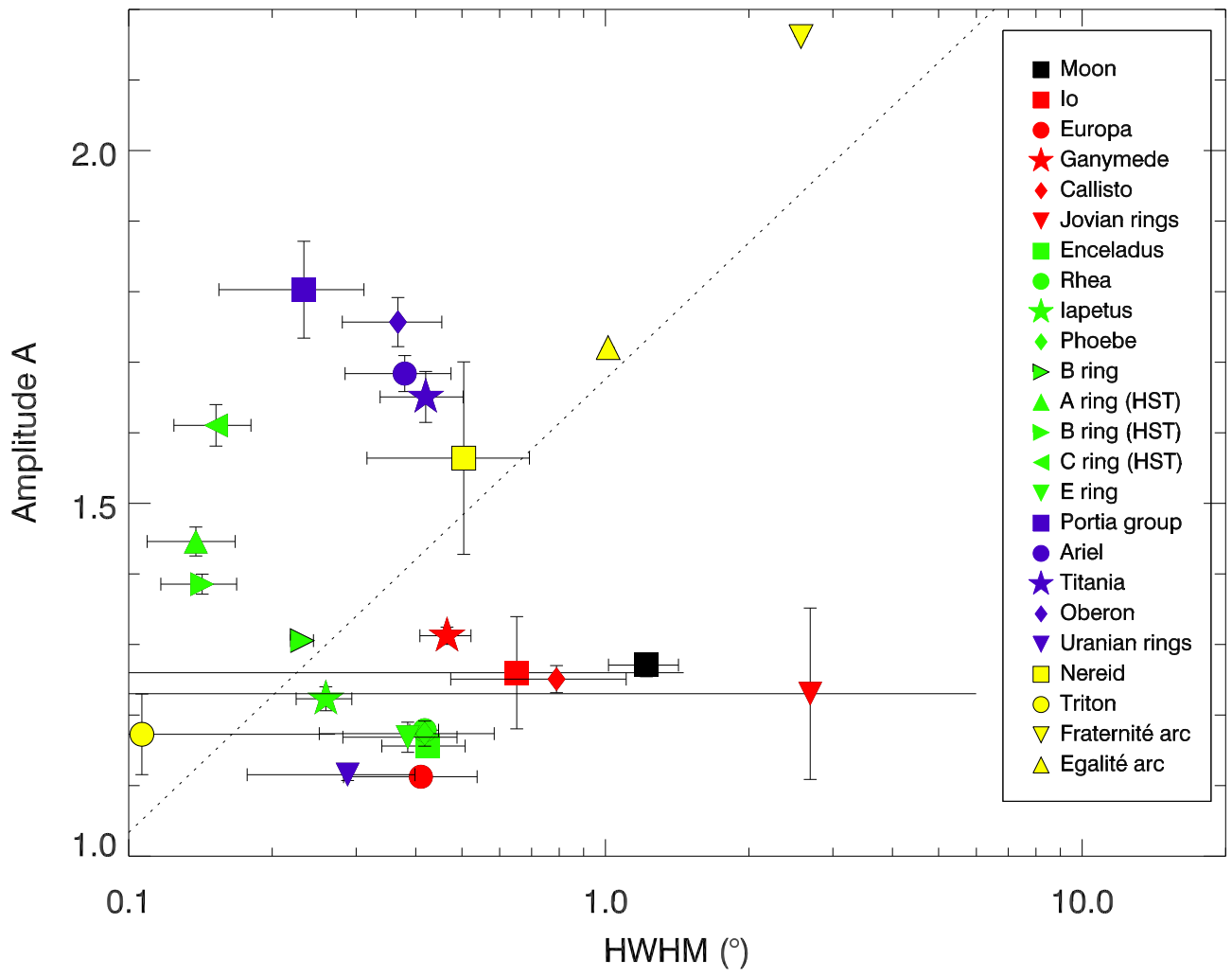
	Object	Solar Angular Size $\alpha_{\odot} (^{\circ})$	Observation Time UT	References
	Moon	0.263	1968 December 24	(Whitaker, 1969)
Jupiter	Main ring	0.0506	2000 December 13	(Throop et al., 2004)
	Io	0.0498	1977 December 15	(Lockwood et al., 1980)
	Europa	0.0515	1976 January 1	(Thompson and Lockwood, 1992)
	Ganymede	0.0499	1971 may 1	(Blanco and Catalano, 1974)
	Callisto	0.0515	1976 January 1	(Thompson and Lockwood, 1992)
Saturn	C ring	0.0295	2005 January 13	(French et al., 2007)
	B ring	0.0266	1959 June 26	(Franklin and Cook, 1965)
	B ring (HST)	0.0295	2005 January 13	(French et al., 2007)
	A ring	0.0295	2005 January 13	(French et al., 2007)
	E ring	0.0271	1980 January 1	(Larson, 1984)
	Enceladus	0.0287	1997 October 10	(Verbiscer et al., 2005)
	Rhea	0.0268	1976 January 13	(Lockwood et al., 1980)
	Iapetus	0.0266	1972 December 1	(Franklin and Cook, 1974)
	Phoebe	0.0295	2005 January 13	(Bauer et al., 2006)
Uranus	Rings	0.0138	1997 July 29	(Karkoschka, 2001)
	Portia <i>group</i>	0.0138	1997 July 29	(Karkoschka, 2001)
	Ariel	0.0138	1997 July 29	(Karkoschka, 2001)
	Titania	0.0138	1997 July 29	(Karkoschka, 2001)
	Oberon	0.0138	1997 July 29	(Karkoschka, 2001)
Neptune	Fraternité	0.00885	2002 July 27	(de Pater et al., 2005)
	Egalité	0.00885	2002 July 27	(de Pater et al., 2005)
	Nereid	0.00889	1998 June 20	(Schaefer and Tourtellotte, 2001)
	Triton	0.00885	1988 June 20	(Buratti et al., 1991)

Table 7

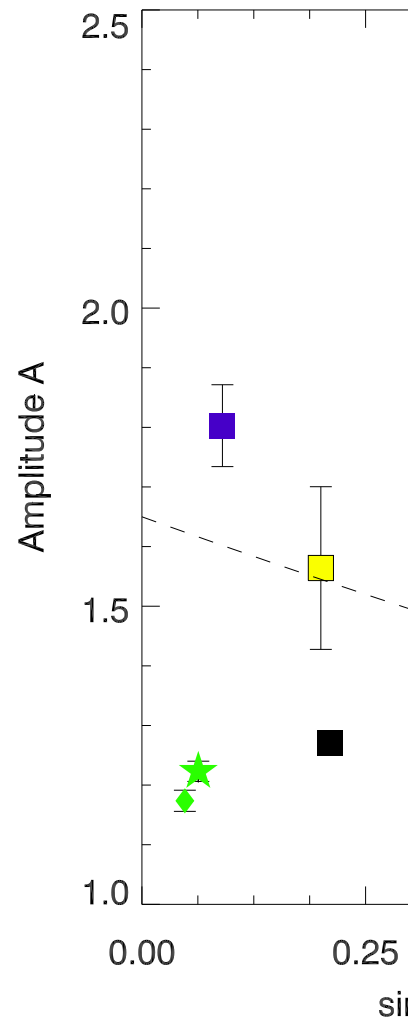
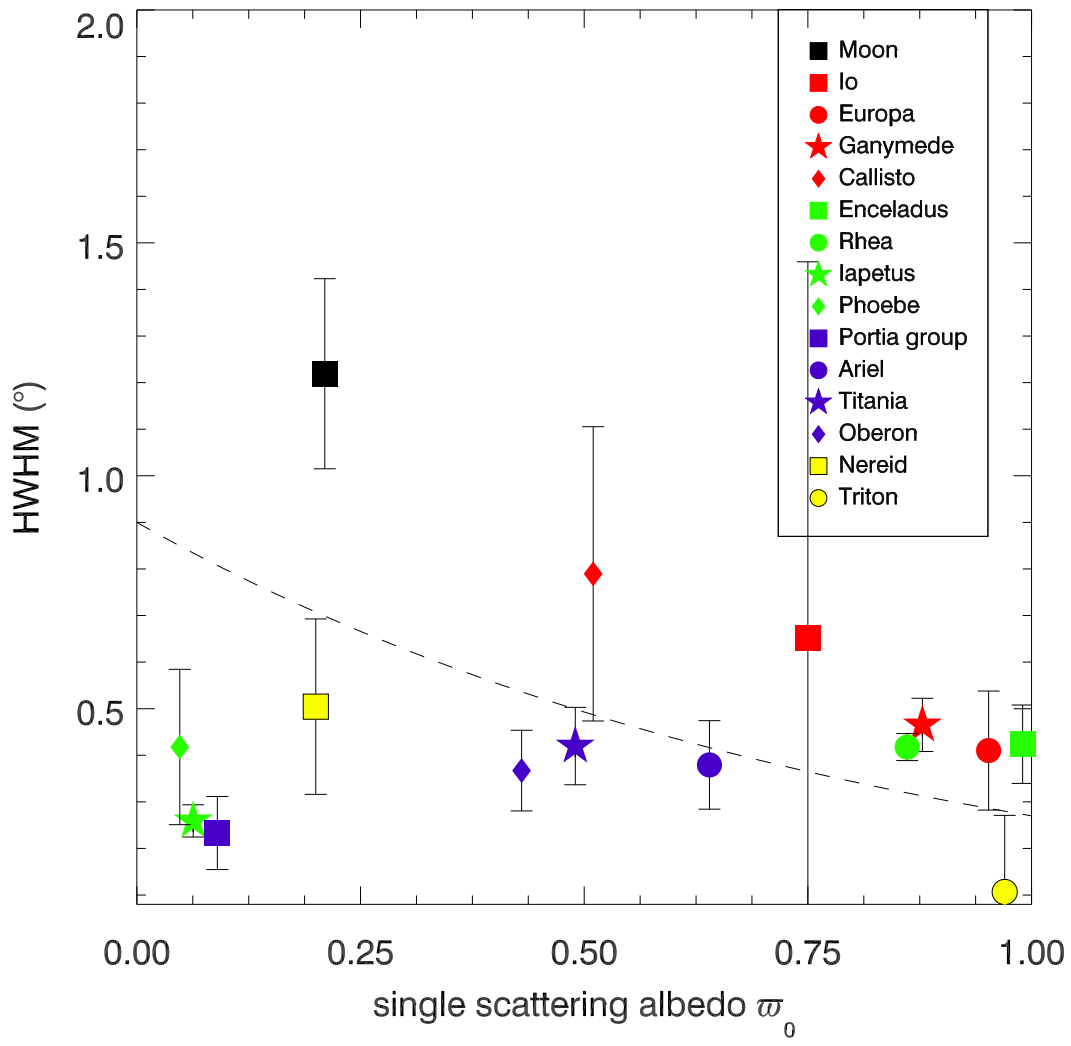
Parameters of the limb darkening function of Pierce and Waddell (1961) at similar wavelengths to the observations.

	Object	λ_{obs} (nm)	Pierce and Waddell (1961)			
			λ (nm)	a_λ	b_λ	c_λ
	Moon	~ 570	560	0.75079	0.41593	-0.54334
Jupiter	Main ring	~ 460	460	0.58274	0.56078	-0.46772
	Io	~ 570	560	0.75079	0.41593	-0.54334
	Europa	~ 500	500	0.68897	0.47873	-0.54651
	Ganymede	~ 600	600	0.78074	0.38427	-0.53777
	Callisto	~ 500	500	0.68897	0.47873	-0.54651
		C ring	672	660	0.83717	0.33283
Saturn	B ring	~ 650	640	0.81999	0.34918	-0.55132
	B ring (HST)	672	660	0.83717	0.33283	-0.55400
	A ring	672	660	0.83717	0.33283	-0.55400
	E ring	~ 650	640	0.81999	0.34918	-0.55132
	Enceladus	439	440	0.49375	0.62584	-0.38974
	Rhea	~ 500	500	0.68897	0.47873	-0.54651
	Iapetus	~ 600	600	0.78074	0.38427	-0.53777
	Phoebe	~ 650	640	0.81999	0.34918	-0.55132
		Rings	~ 500	500	0.68897	0.47873
Uranus	Portia <i>group</i>	~ 500	500	0.68897	0.47873	-0.54651
	Ariel	~ 600	600	0.78074	0.38427	-0.53777
	Titania	~ 600	600	0.78074	0.38427	-0.53777
	Oberon	~ 600	600	0.78074	0.38427	-0.53777
		Fraternité	~ 500	500	0.68897	0.47873
Neptune	Egalité	~ 500	500	0.68897	0.47873	-0.54651
	Nereid	~ 570	560	0.75079	0.41593	-0.54334
	Triton	~ 400	400	0.16732	0.84347	-0.03516

Liner-by-part



(a) Angular width



(a)

